Research Square

Preprints are preliminary reports that have not undergone peer review.
They should not be considered conclusive, used to inform clinical practice,
or referenced by the media as validated information.

Seismic Compositional Constraints on the Zhongnan Fault and Ridge Zone from the relict spreading ridge to the southern continental margin of the South China Sea

Weiye Si
Zhejiang University
Chun-Feng Li
cfli@zju.edu.cn

Zhejiang University
Wang Li
Zhejiang University
Yongjian Yao
Ministry of Natural Resources, Guangzhou Marine Geological Survey
Min Xu
Chinese Academy of Sciences
Chuanhai Yu
Chinese Academy of Sciences
Yongkang Deng
Zhejiang University
Ming Yang
Zhejiang University
Jinwei Gao
Chinese Academy of SciencesInstitute of Deep-Sea Science and Engineering

Research Article

Keywords: Zhongnan Fault and Ridge Zone, lower-crustal high-velocity bodies, ocean bottom seismometer, S-wave velocity, Vp/Vs ratio, South China Sea

Posted Date: November 24th, 2026

DOI: https://doi.org/10.21203/rs.3.rs-11679213/v1

License: This work is licensed under a Creative Commons Attribution 4.0 International License.
Read Full License

Additional Declarations: No competing interests reported.

Seismic Compositional Constraints on the Zhongnan Fault and Ridge Zone from the relict spreading ridge to the southern continental margin of the South China Sea

Weiye Si [a,f], Chun-Feng Li [a,b,c*], Wang Li [a], Yongjian Yao [d], Min Xu [e], Chuanhai Yu [e], Yongkang Deng [a], Ming Yang [f], Jinwei Gao [g]

[a] Department of Marine Sciences, Zhejiang University, Zhoushan 316021, China

[b] Institute of Fundamental and Transdisciplinary Research, Zhejiang University, Hangzhou 310058, China

[c] State Key Laboratory of Ocean Sensing, ZJU-Hangzhou Global Scientific and Technological Innovation Center, Zhejiang University, Hangzhou, 311215, China

[d] Key Laboratory of Submarine Mineral Resources, Ministry of Natural Resources, Guangzhou Marine Geological Survey, Guangzhou 510760, China

[e] State Key Laboratory of Tropical Oceanography, South China Sea Institute of Oceanology, Chinese Academy of Sciences, Guangzhou 510301, China

[f] Hainan Institute, Zhejiang University, Sanya 572025, Hainan, China

[g] Laboratory of Marine Geophysics and Georesources, Institute of Deep-Sea Science and Engineering, Chinese Academy of Sciences, Sanya, Hainan 572000, China

(* Corresponding author: Chun-Feng Li, Email: cfli@zju.edu.cn)

Abstract

The Zhongnan Fault and Ridge Zone between the East and Southwest Sub-basin of the South China Sea, as well as its adjacent continent–ocean transition (COT) near the Reed Bank, are key tectono-magmatic units in the South China Sea. Their P-wave velocities (Vp) have recently been investigated along profile OBS2023-1. To adequately constrain crustal lithology or the origin of anomalous velocity bodies, we use converted S-wave arrivals recorded along the same profile to build an S-wave velocity (Vs) model through both forward

modeling and travel-time tomography. We then derive the Vp/Vs structure and further constrain crustal composition and the nature of deep-seated velocity anomalies. Sedimentary S-wave velocities range from 0.2 to 0.9 km/s, with Vp/Vs > 2.50. Crustal S-wave velocities range from 2.4 to 4.4 km/s, and crustal and upper-mantle Vp/Vs ratios range from 1.70 to 1.90. These results are conformable with a typical basaltic upper crust and a diabasic–gabbroic lower crust in the oceanic domain, and with shallow felsic compositions and deep mafic compositions of the thinned continental crust. The COT displays more complex Vp–Vs relationships: its upper crust has both continental and oceanic lithological affinities, whereas its lower crust is predominantly mafic, indicating a composite crustal structure. Lower-crustal high-velocity bodies identified within the oceanic crust and the COT with Vp > 7.3 km/s, Vs > 4.0 km/s, and Vp/Vs of 1.80–1.90 are consistent with maficlower-crustal intrusion and localized underplating. A volcanic structure between OBS06 and OBS07 overlies a crustal high-Vp/Vs zone that extends upward to the basement and may indicate the extent of magma migration. This area lies within the tectonically complex Zhongnan Fault Zone, where associated deep faults could also have facilitated seawater infiltration and localized mantle hydration near its lower end, suggesting that fault-controlled magma and fluid migration may have further modified the deep structure within the Zhongnan Fault and Ridge Zone.

Keywords: Zhongnan Fault and Ridge Zone; lower-crustal high-velocity bodies; ocean bottom seismometer; S-wave velocity; Vp/Vs ratio; South China Sea

1 Introduction

The Zhongnan Fault and Ridge Zone between the East and Southwest Sub-basin of the South China Sea and the adjacent southeast continent–ocean transition zone (COT) near the Reed Bank are key features for understanding continental breakup, seafloor spreading, and subsequent magmatic modification in the southern South China Sea(Li and Song 2012; Li 1997; Peng et al. 2020). The Zhongnan Fault and Ridge Zone is more than a simple tectonic boundary: it exhibits pronounced variations in crustal structure and lower-crustal high-velocity anomalies that may reflect faulting, magmatic intrusion, and subsequent tectonic reactivation (Li et al. 2026). The deep structures of this zone and the adjacent COT are therefore essential to understanding their roles in the evolution of the southern South China Sea margin.

Wide-angle seismic studies using ocean-bottom seismometers (OBSs) constrain the physical properties of the crust and upper mantle through P-wave and S-wave velocities. P-wave velocity models can characterize crustal affinity and velocity anomalies. Vp/Vs ratio is more sensitive to rock composition and provides an important seismological constraint on lithology (Carlson and Miller 1997; Christensen 2004, 1996; Grevemeyer et al. 2018a, b; Kodaira et al. 1996). Joint interpretation of Vp, Vs, and Vp/Vs therefore helps distinguish geological processes, such as mafic magmatic underplating and serpentinization, that may produce similar P-wave velocity ranges.

Such multiparameter constraints are particularly valuable in the tectonically and magmatically complex Zhongnan Fault and Ridge Zone and COT. Lower-crustal high-velocity bodies along the southern margin were less studied than in the northern conjugate margin (Pichot et al. 2014; Chang et al. 2017; Peng et al. 2020), and their origin remains debated (Yu et al. 2017; Li et al. 2021a, b). How could magmatism along the Zhongnan

Fault and Ridge Zone system and in the adjacent COT be controlled by faults? Are deep high-velocity anomalies spatially associated with shallow magmatic or volcanic activity? Does localized mantle hydration occur within the Zhongnan Fault and Ridge Zone?

To address these questions, we use converted S-wave arrivals from OBS profile OBS2023-1 to obtain high-resolution Vs and Vp/Vs structures of the extinct spreading ridge, Zhongnan Fault and Ridge Zone, normal oceanic crust, COT, and continental crust within a consistent framework for data processing and velocity parameterization. We examine whether high Vp/Vs structures in different tectonic domains share similar spatial positions, dimensions, and origins. We also constrain whether mafic magmatic intrusion and localized mantle hydration coexist under the influence of transform faulting.

2 Geological Setting and Previous OBS Surveys

The South China Sea lies near the junction of the Eurasian, Indo-Australian, and Philippine Sea plates and is a typical Cenozoic marginal sea of the western Pacific. Between approximately 33 and 15 Ma, the South China Sea margin underwent multiple phases of extension and spreading (Li et al. 2014), forming the East, Northwest, and Southwest Sub-basins in succession. The Southwest Sub-basin formed at approximately 23.6–16 Ma. Repeated changes in spreading direction and rate, accompanied by migration of the spreading center and transform faulting, substantially influenced basin geometry and crustal structure (Briais et al. 1993; Li and Song 2012; Sibuet et al. 2016).

The study area is located at the transition between the Southwest Sub-basin, the East Sub-basin, and the Reed Bank margin (Fig. 1). Profile OBS2023-1 trends approximately northwest–southeast and crosses, in sequence, the extinct spreading ridge, the Zhongnan Fault and Ridge Zone, oceanic crust, the COT, and the continental crust of the Reed Bank in the southern South China Sea margin.

Recent OBS wide-angle seismic studies have progressively revealed the complex S-wave velocity deep structure of the South China Sea margins. Wei et al. (2015) derived a converted S-wave velocity model for the Reed Bank and the adjacent ocean basin. Guo et al. (2023) further resolved the converted S-wave structure beneath the Liyuexi Trough and COT, and identified lithological characteristics transitional between continental and oceanic crust, and a lower-crustal high-velocity layer (Vs ~ 4.0–4.2 km/s) of amphibolitic magmatic underplating. These studies suggest that the Reed Bank and its adjacent COT have undergone substantial tectonic extension and magmatic modification.

In the northwestern conjugate margin, Li et al. (2022, 2021a) constructed Vp/Vs models across the Zhongsha Block and the adjacent COT. The upper crust was of felsic lithologies, including andesite, granite, and granodiorite, whereas the lower crust was dominated by greenschist with minor anorthosite. The COT was interpreted primarily as fragmented, extended continental crust modified by magmatism, with possible mafic intrusions at depth. Farther seaward, the upper mantle beneath thin oceanic crust locally shows evidence of partial serpentinization.

Based on independent P- and S-wave tomography across the extinct spreading ridge in the East Sub-basin, Jiang et al. (2025) identified thin oceanic crust of approximately 3.3–4.3 km thick and Vp/Vs anomalies

exceeding 1.90, and proposed that waning magma supply, enhanced tectonic extension, and throughgoing faulting during the final stages of spreading jointly promoted seawater infiltration and upper-mantle hydration. To address complex converted-wave ray paths and inconsistent identification of conversion interfaces, Wen et al. (2024) demonstrated the feasibility of using travel-time-corrected converted S-waves for Vs tomography.

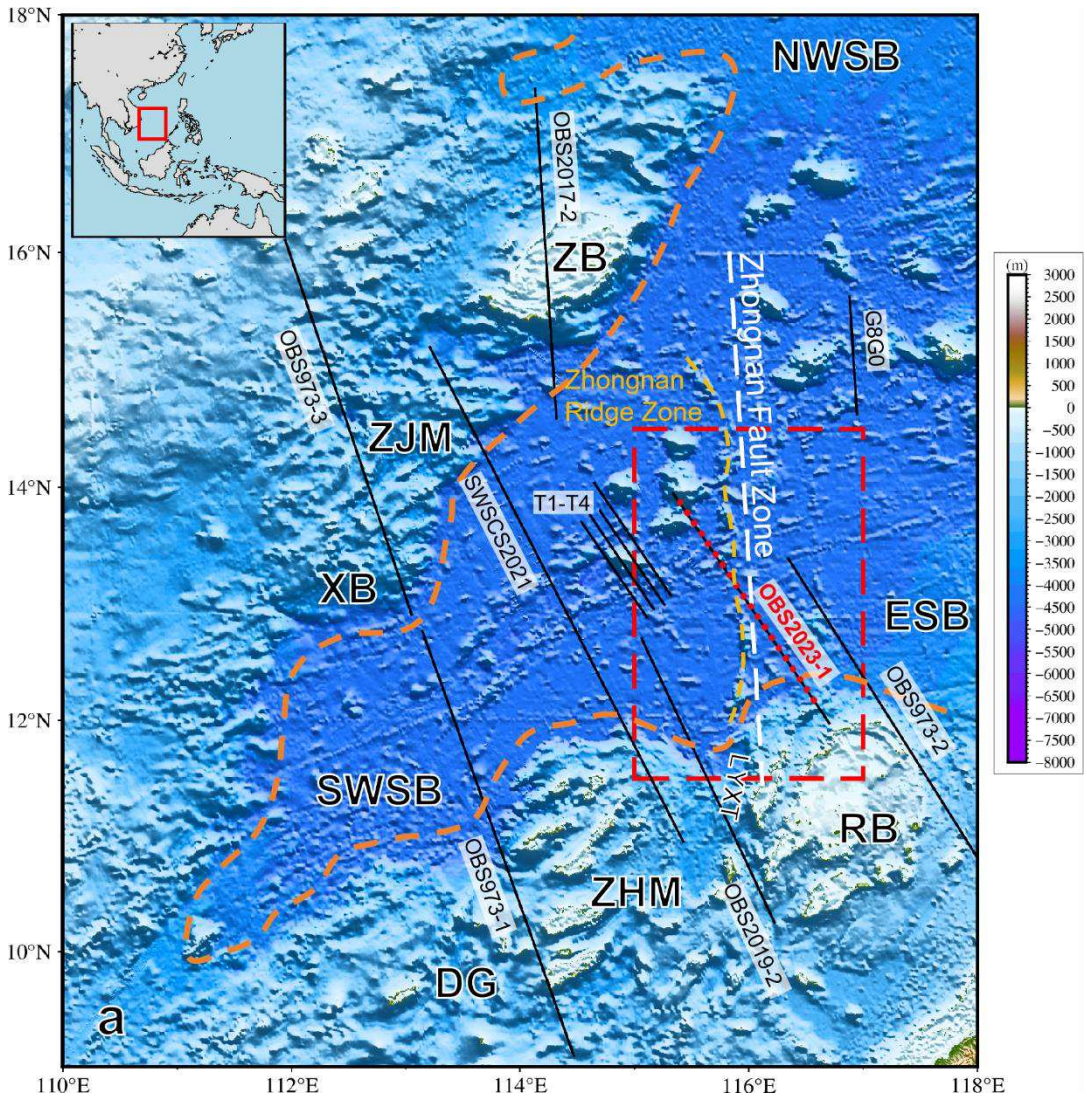

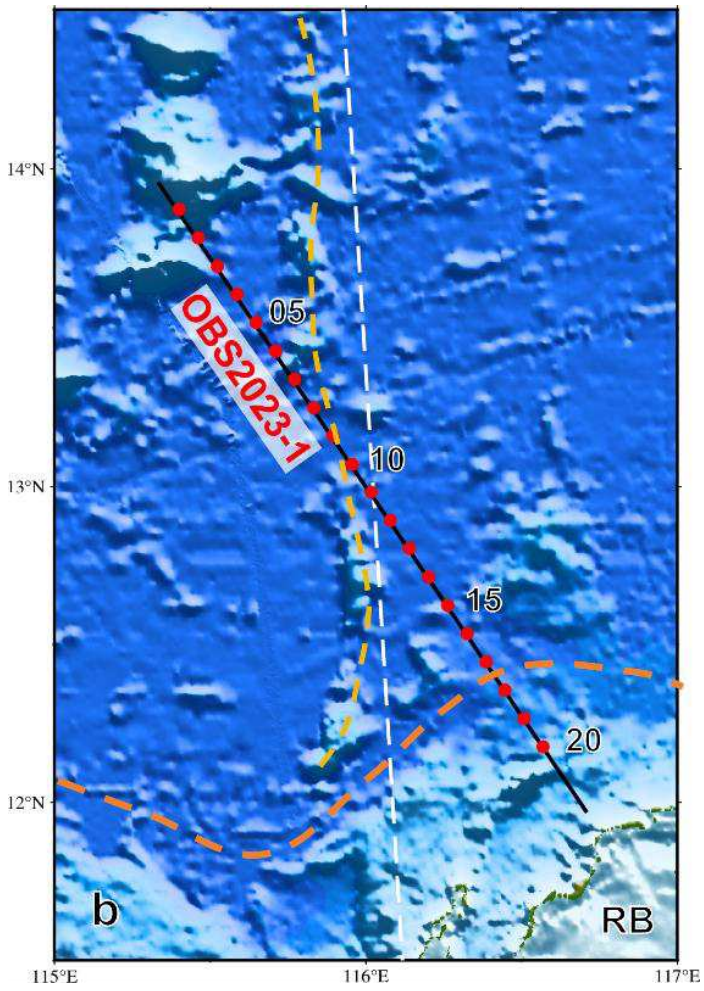

Figure 1. Bathymetric map of the study area. (a) Tectonic domains and seismic profiles. OBS2023-1, marked by 20 red circles, is the seismic profile used in this study. Thin black lines show previous wide-angle seismic profiles (Guo et al. 2023; Jiang et al. 2025; Li et al. 2022, 2021a; Zhang et al. 2020; Wei et al. 2015; Zhang et al. 2025; Qiu et al. 2011). White and yellow dashed lines mark the Zhongnan Fault and Ridge Zone, respectively (Li and Song 2012). The orange dashed line marks the continent–ocean boundary (Song et al. 2019). The red dashed box outlines panel (b). (b) Station distribution along OBS2023-1. Red circles indicate the locations of the 20 OBS stations. ZB, Zhongsha Block; RB, Reed (Liyue) Bank; ZJM, Zhongjian Massif; ZHM, Zhenghe Massif; XB, Xisha Block; DG, Dangerous Ground (Nansha Block); NWSB, Northwest Sub-basin; SWSB, Southwest Sub-basin; ESB, East Sub-basin. LYXT, Liyuexi Trough.

3 Data acquisition and preprocessing

The OBS2023-1 geophysical survey was conducted aboard R/V Shiyan 6, operated by the South China Sea Institute of Oceanology, Chinese Academy of Sciences. A number of 20 OBSs were successfully deployed and recovered along the 245-km profile, with a nominal station spacing of approximately 12 km. The source array comprised four large-volume airguns with a total volume of 6,000 in^3, towed at a depth of 10 m. The array was fired every 50 s at an operating pressure of 11–12 MPa, giving a shot spacing of ~125 m. A total number of 1,949 valid shots were acquired.

A coincidental 280-km MCS reflection profile was also acquired during the survey. The MCS source consisted of a 4,000-in^3 airgun array operated at 2,000 psi (approximately 13.8 MPa). Data were recorded using a 6-km streamer with a channel spacing of 12.5 m and a shot spacing of 37.5 m.

Seismic data preprocessing included data format conversion, shot-time and shot-position corrections, OBS clock and position corrections, bandpass filtering, and gain (Li et al. 2026). The horizontal components of free-fall OBSs are generally misaligned with the source–receiver direction. To improve S-wave data quality, we rotated the horizontal recordings into radial and transverse components, parallel and perpendicular to the source–receiver direction, respectively. For each OBS, an energy-scanning method (Zhang et al. 2016) was used to determine the rotation angle that maximized S-wave energy. After rotation, S-wave energy was more concentrated on the radial component (Fig. 2).

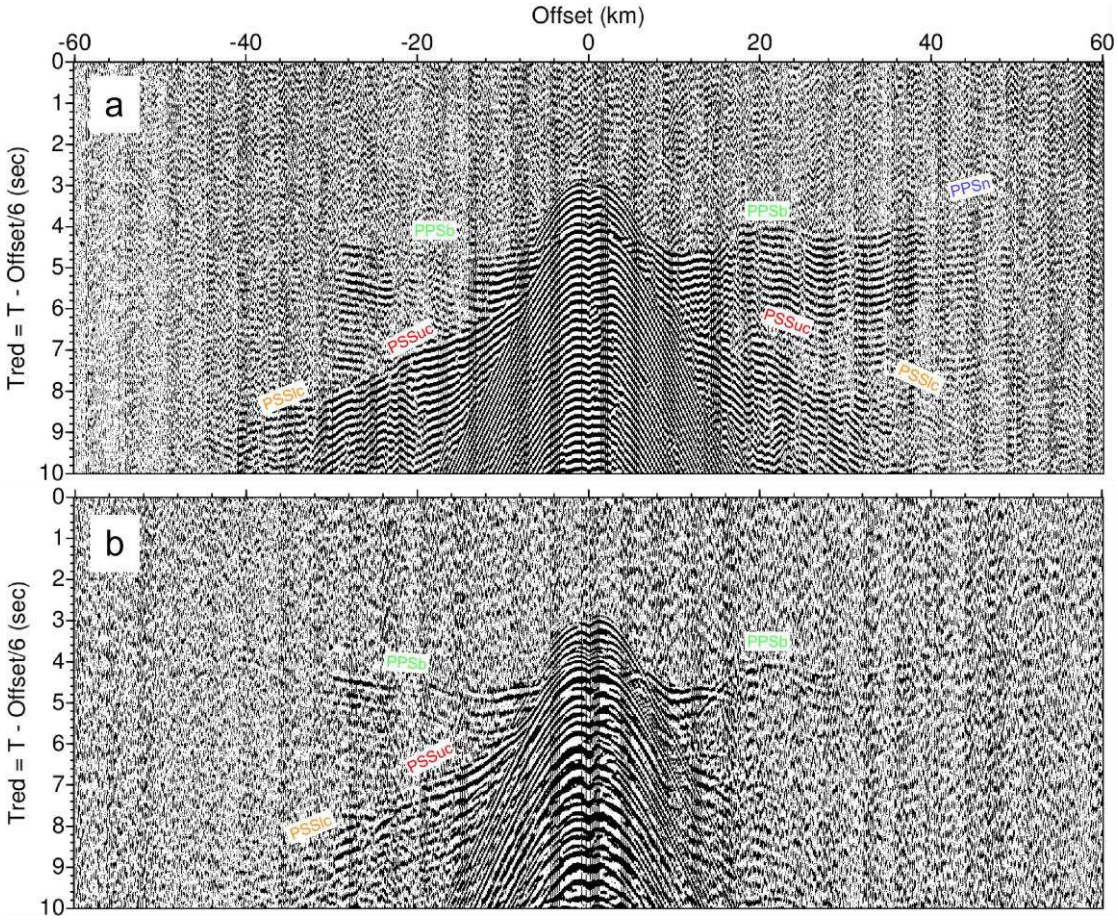

Figure 2. Comparison of the (a) radial and (b) transverse components at station OBS05.

4 S-wave forward modeling and inversion

4.1 S-wave types and identification

Because seawater cannot transmit S-waves, S-waves recorded by OBSs originate from P-to-S conversion at subsurface interfaces (Digranes et al. 1998). Conversion commonly occurs at interfaces with strong contrasts in lithology and velocity, such as the seafloor, sediment–basement interface, and Moho (Mjelde et al. 2003; Zhao et al. 2010). Two conversion modes are considered: PPS-type waves, generated when upgoing P-waves convert to S-waves, and PSS-type waves, generated when downgoing P-waves convert to S-waves (Kodaira et al. 1996) (Fig. 3).

Converted S-waves are identified primarily from their arrival-time differences relative to P-waves and from particle-motion trajectories (Digranes et al. 1998; Zhao et al. 2008). PPS arrivals generally follow their

corresponding P-wave arrivals by a relatively short interval, whereas PSS arrivals have a larger delay. For example, at station OBS10, Pg arrives at approximately 3.8 s (Fig. 4a), PPS at approximately 5.2 s, and PSS at approximately 7.0 s (Fig. 4b). P-wave particle motion is predominantly vertical (Fig. 4c), whereas S-wave particle motion is predominantly horizontal along the radial direction (Fig. 4d–e).

Examples of S-wave phase identification and travel-time fitting are shown in Figs. 5–7. Two PPS-type phases were identified: PPSb and PPSn, generated by conversion of upgoing Pg and Pn waves, respectively, at the sediment–basement interface. Three PSS-type phases were identified: PSSuc, PSSlc, and PSSn. PSSuc and PSSlc correspond to downgoing P-to-S conversion at the sediment–basement interface along crustal paths associated with Pg; the former samples the upper crust and the latter the lower crust. PSSn corresponds to downgoing P-to-S conversion at the sediment–basement interface along a mantle-refracted path associated with Pn, followed by S-wave propagation through the upper mantle and back to the receiver. Table 1 summarizes the root-mean-square (RMS) residuals and other statistics for all phases.

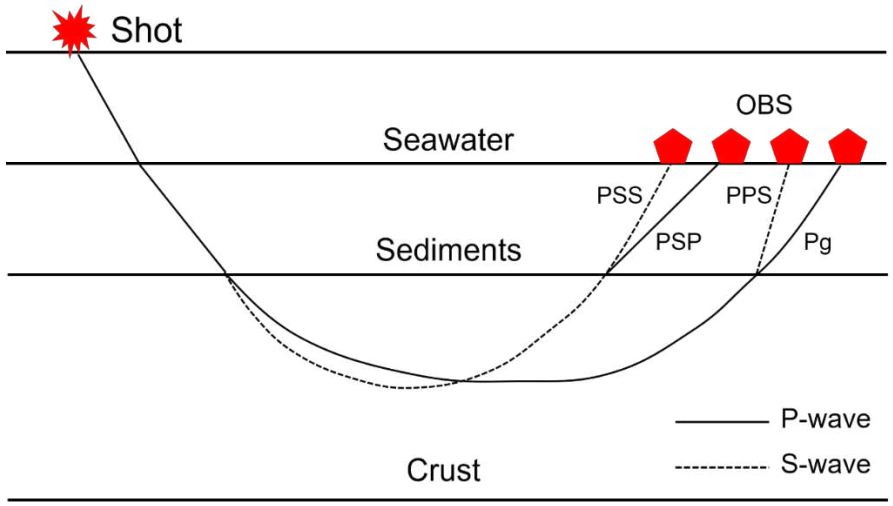

Figure 3. Converted-wave types generated at the sediment–basement interface. Pg, crustal refracted P-wave; PSP, PPS, and PSS, converted S-waves.

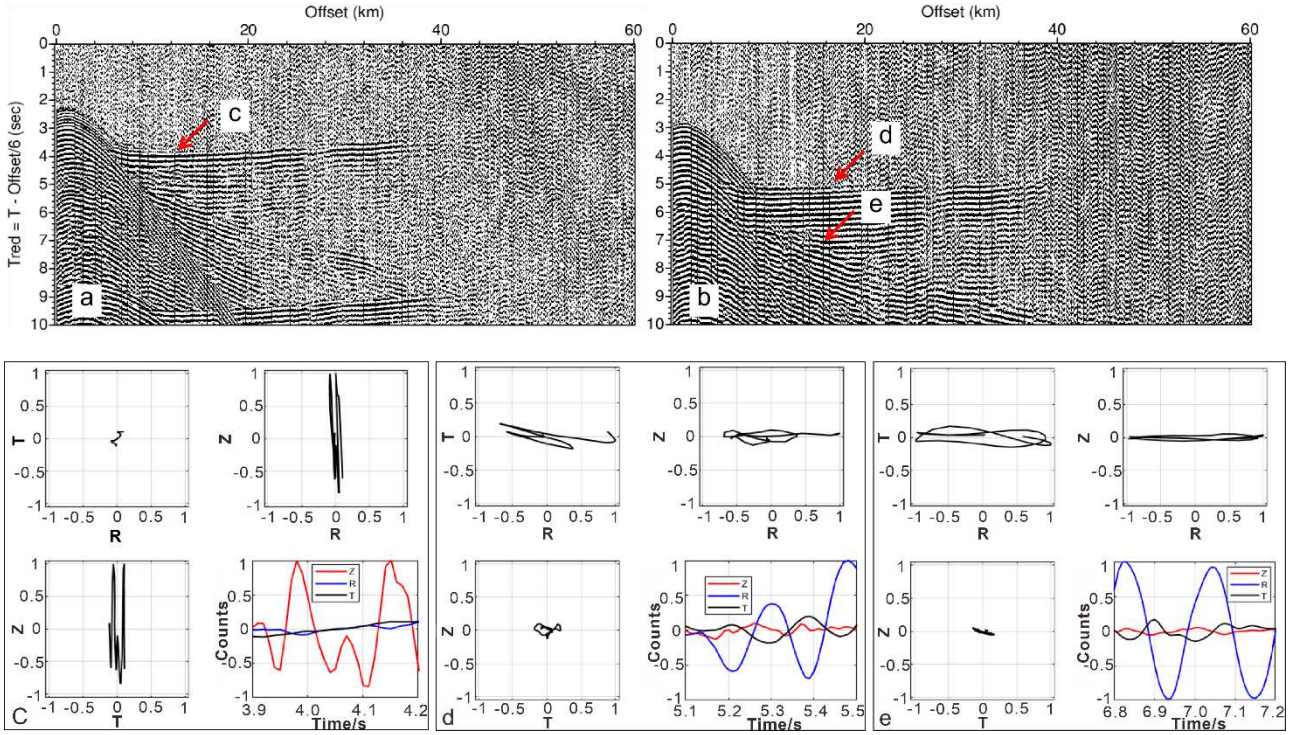

Figure 4. (a) Vertical and (b) radial components at station OBS10, plotted with a reduction velocity of 6 km/s. Arrows indicate the (c) P-wave, (d) PPS, and (e) PSS arrivals, with their corresponding particle-motion trajectories.

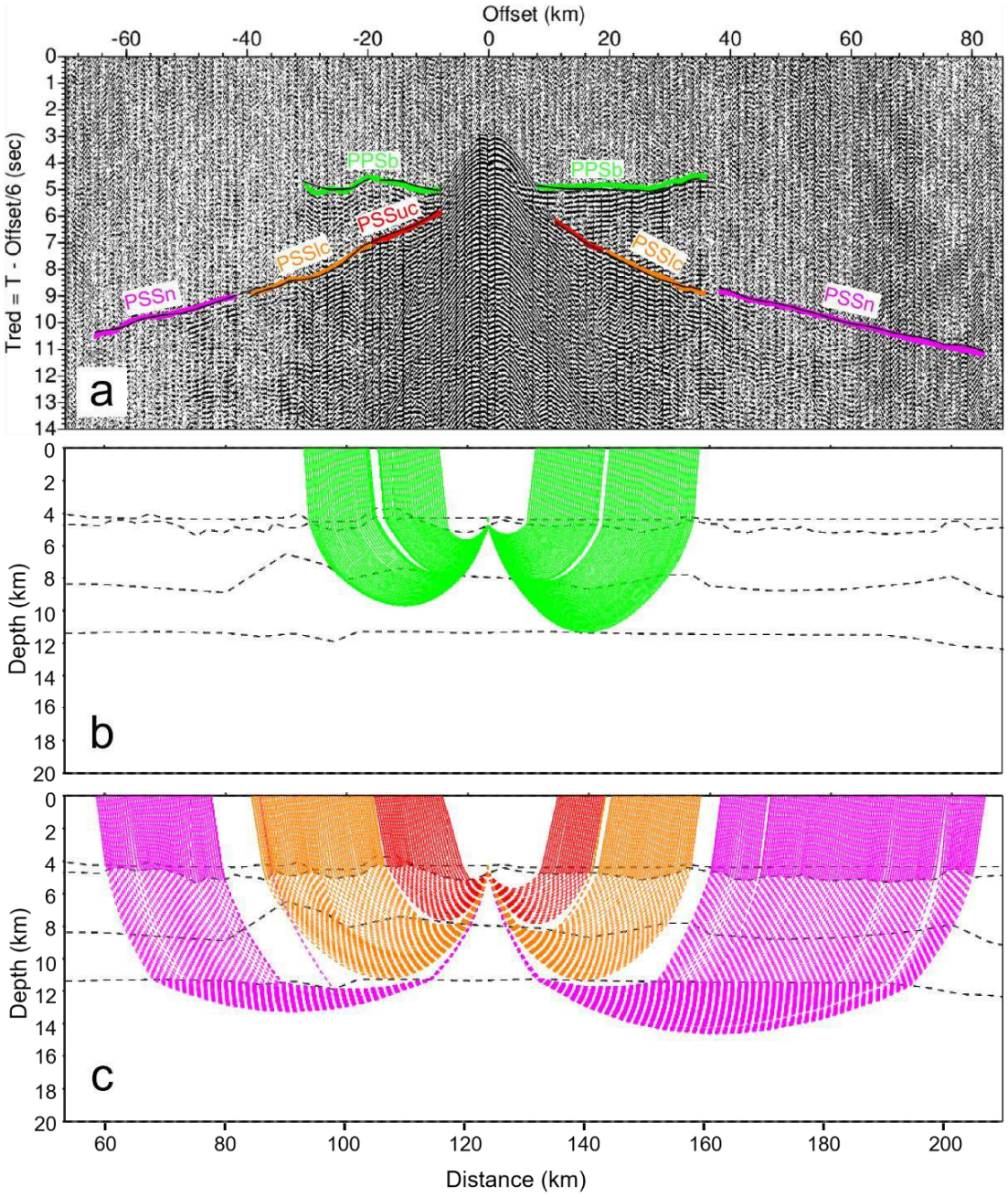

Figure 5. (a) Radial-component record section and converted S-wave phases at OBS08, plotted with a reduction velocity of 6 km/s. Colored curves indicate travel-time for different phases. (b) Calculated ray paths for PPS arrivals. (c) Calculated ray paths for PSS arrivals. Solid and dashed lines represent P- and S-wave ray segments, respectively.

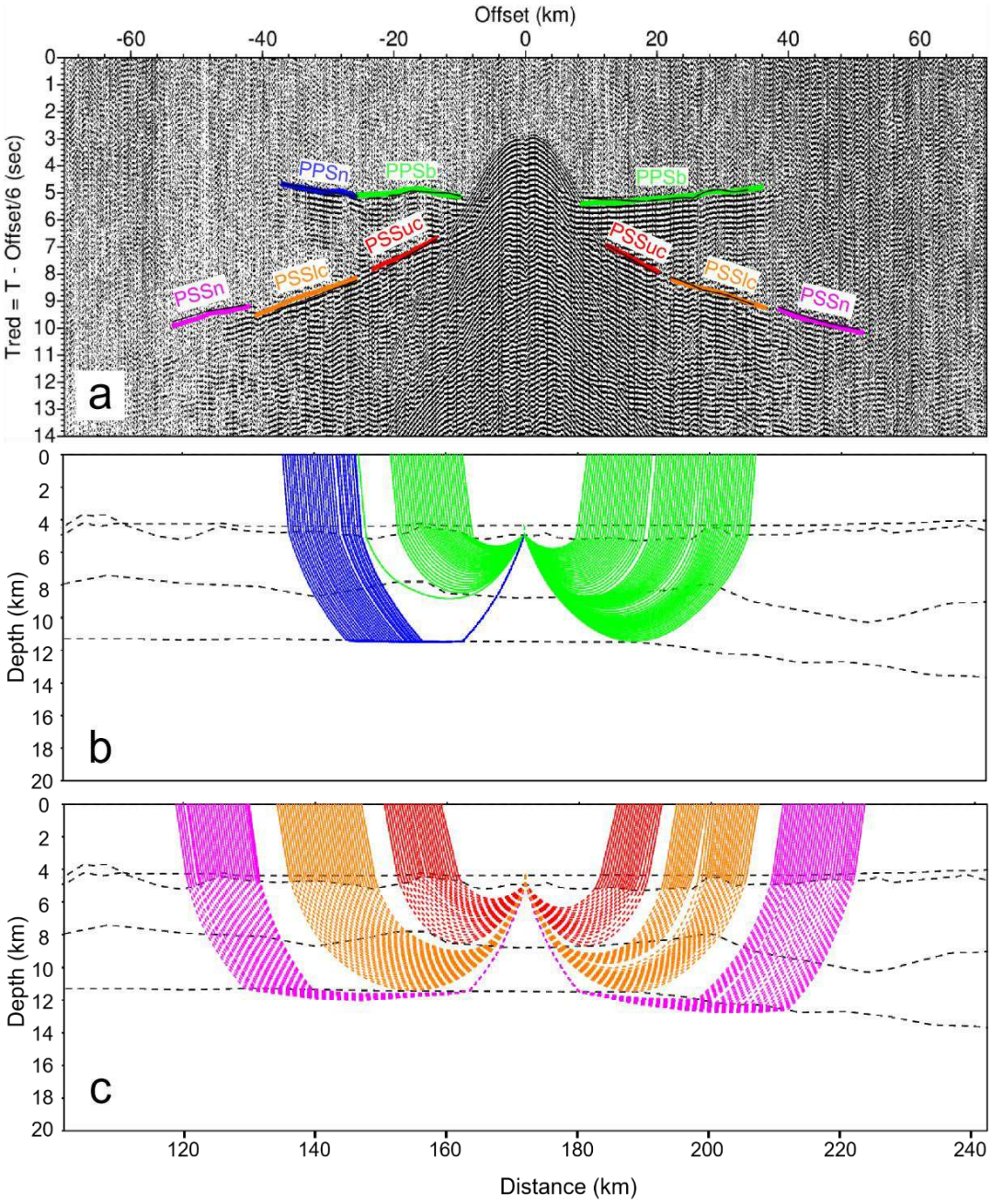

164

165 Figure 6. (a) Radial-component record section and converted S-wave phases at OBS12, plotted with a reduction velocity
166 of 6 km/s. Colored curves indicate travel-time for different phases. (b) Calculated ray paths for PPS arrivals. (c)
167 Calculated ray paths for PSS arrivals. Solid and dashed lines represent P- and S-wave ray segments, respectively.

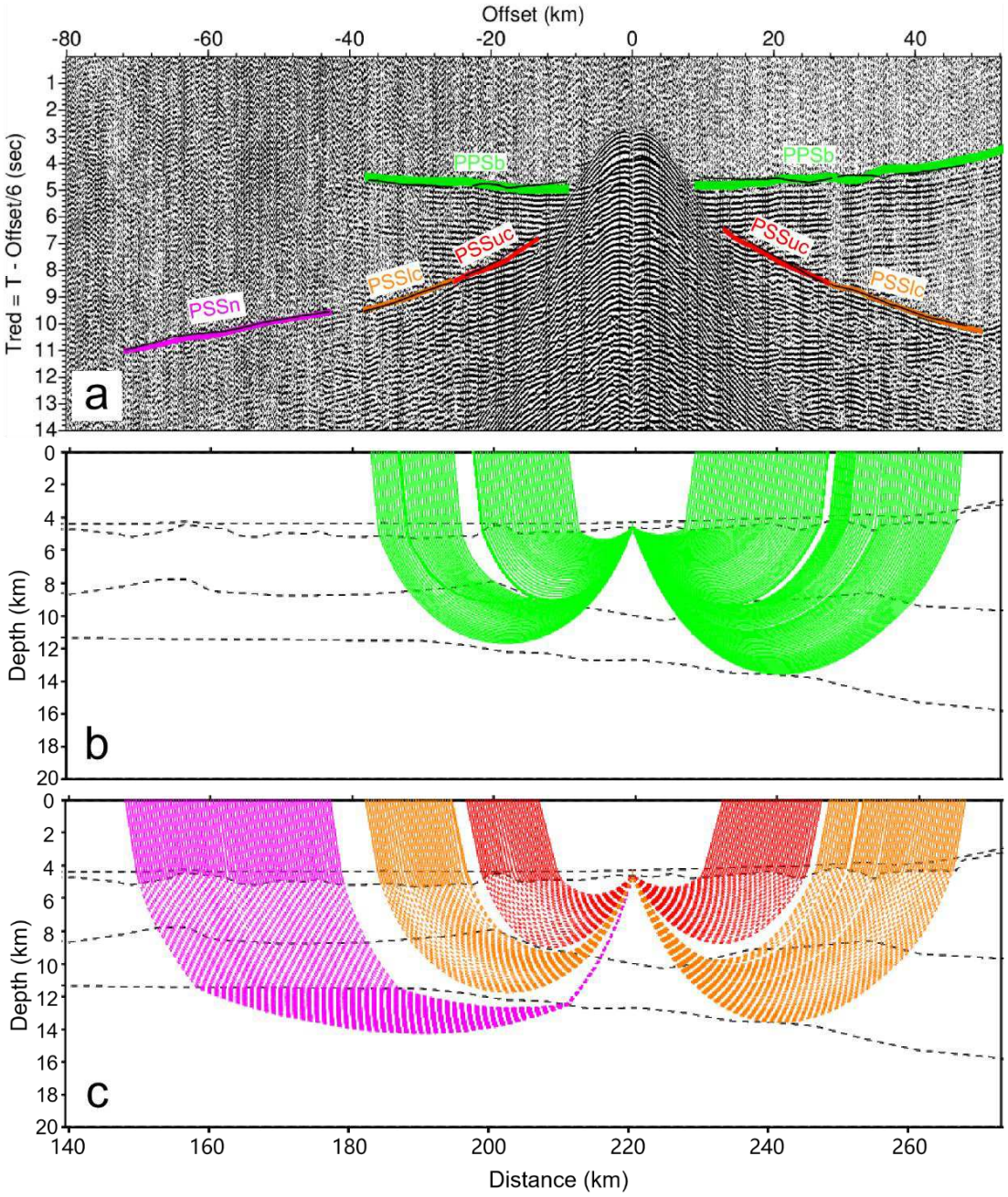

Figure 7. (a) Radial-component record section and converted S-wave phases at OBS16, plotted with a reduction velocity of 6 km/s. Colored curves indicate travel-time for different phases. (b) Calculated ray paths for PPS arrivals. (c) Calculated ray paths for PSS arrivals. Solid and dashed lines represent P- and S-wave ray segments, respectively.

4.2 S-wave forward ray-tracing modeling

S-wave forward modeling followed the same approach as P-wave modeling, progressing from individual stations to multiple stations, from shallow to deep structure, and from short to long offsets. Ray tracing was performed using RayInvr (Zelt and Smith 1992). The P-wave velocity structure served as the initial model, with interface depths and Vp held fixed. Each layer was divided into hundreds of blocks, and the existing discontinuities were retained as candidate P-to-S conversion interfaces. For each picked phase, Poisson's ratios in the blocks traversed by its ray paths and the choice of conversion interface were adjusted by trial and error

until the calculated and observed travel-time match closely (Figs. 8–9). The resulting Poisson's ratios and Vp were then used to calculate the S-wave velocity (Fig. 10b) and Vp/Vs (Fig. 10c). The forward Vs model yields sedimentary velocities of 0.2–0.9 km/s, upper-crustal velocities of 2.4–3.6 km/s, and lower-crustal velocities of 3.6–4.4 km/s. The forward Vp/Vs model gives ratios of 1.77–1.86 in the upper crust and 1.76–1.85 in the lower crust.

The RMS residuals for the modeled S-wave phases are below 120 ms, averaging approximately 107 ms, and χ^2 values are below 1.8, averaging approximately 1.2 (Table 1). The sediment–basement interface is the principal conversion boundary for all phases. S-wave ray coverage exceeds 50-fold over most parts of the model (Figs. 8–9). The overall good agreement between observed and calculated travel-time warrants the accuracy and reliability of the forward model.

Table 1. Forward-modeling statistics for converted S-waves along profile OBS2023-1.

Phases	**Uncertainty(ms)**	**Number of picks**	**RMS (s)**	**χ^2**	**Mode**	**P-S interface**
PPSb	90-150	6792	0.109	1.197	PPS	Basement
PPSn	90	1350	0.108	1.439	PPS	Basement
PSSuc	90-150	2393	0.114	1.440	PSS	Basement
PSSlc	90-150	4365	0.086	0.868	PSS	Basement
PSSn	90	2448	0.120	1.775	PSS	Basement

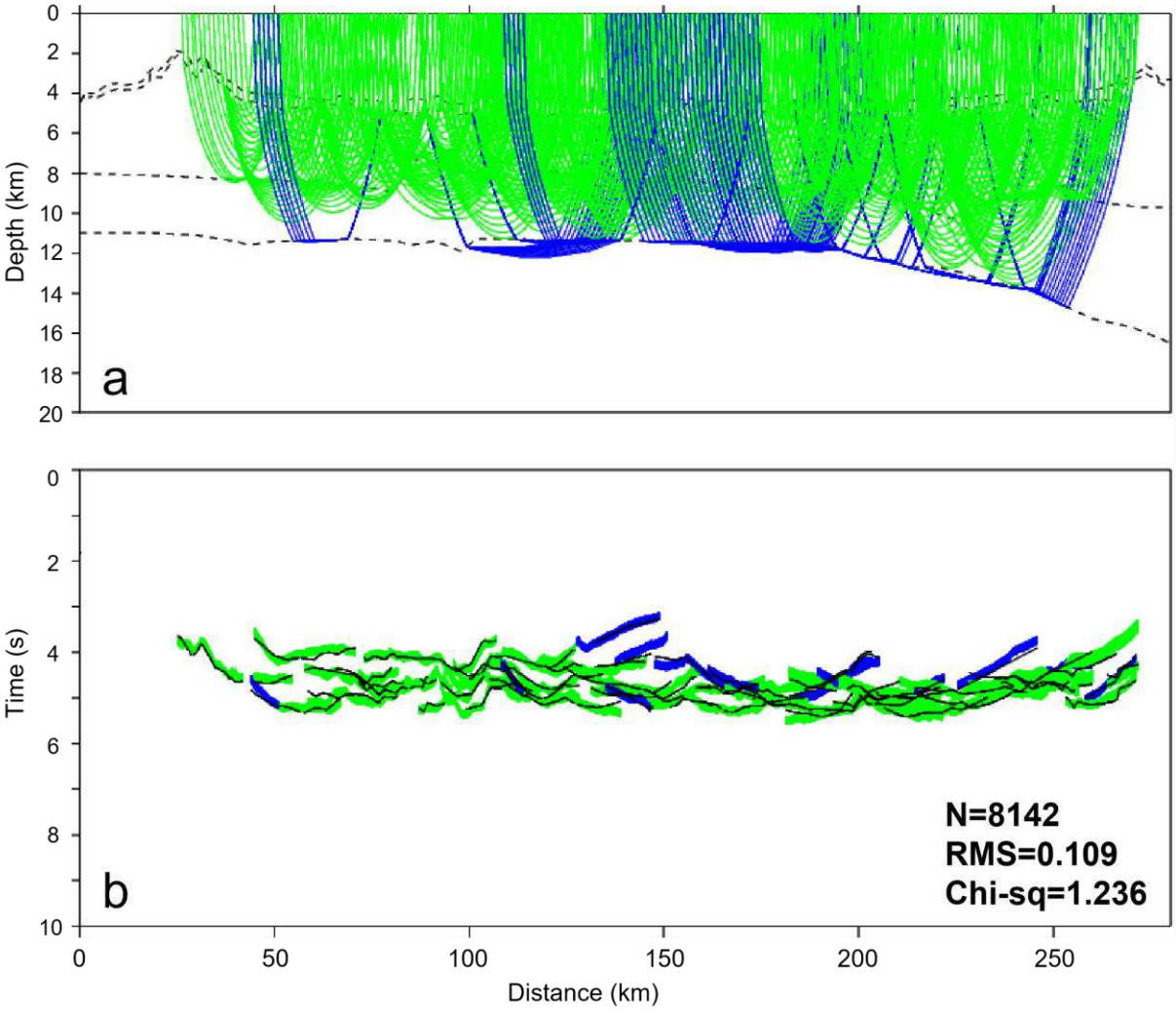

191

192 Figure 8. (a) Ray paths for all PPS converted S-wave phases. (b) Observed (colored) and calculated (black) travel-time
193 for PPS phases.

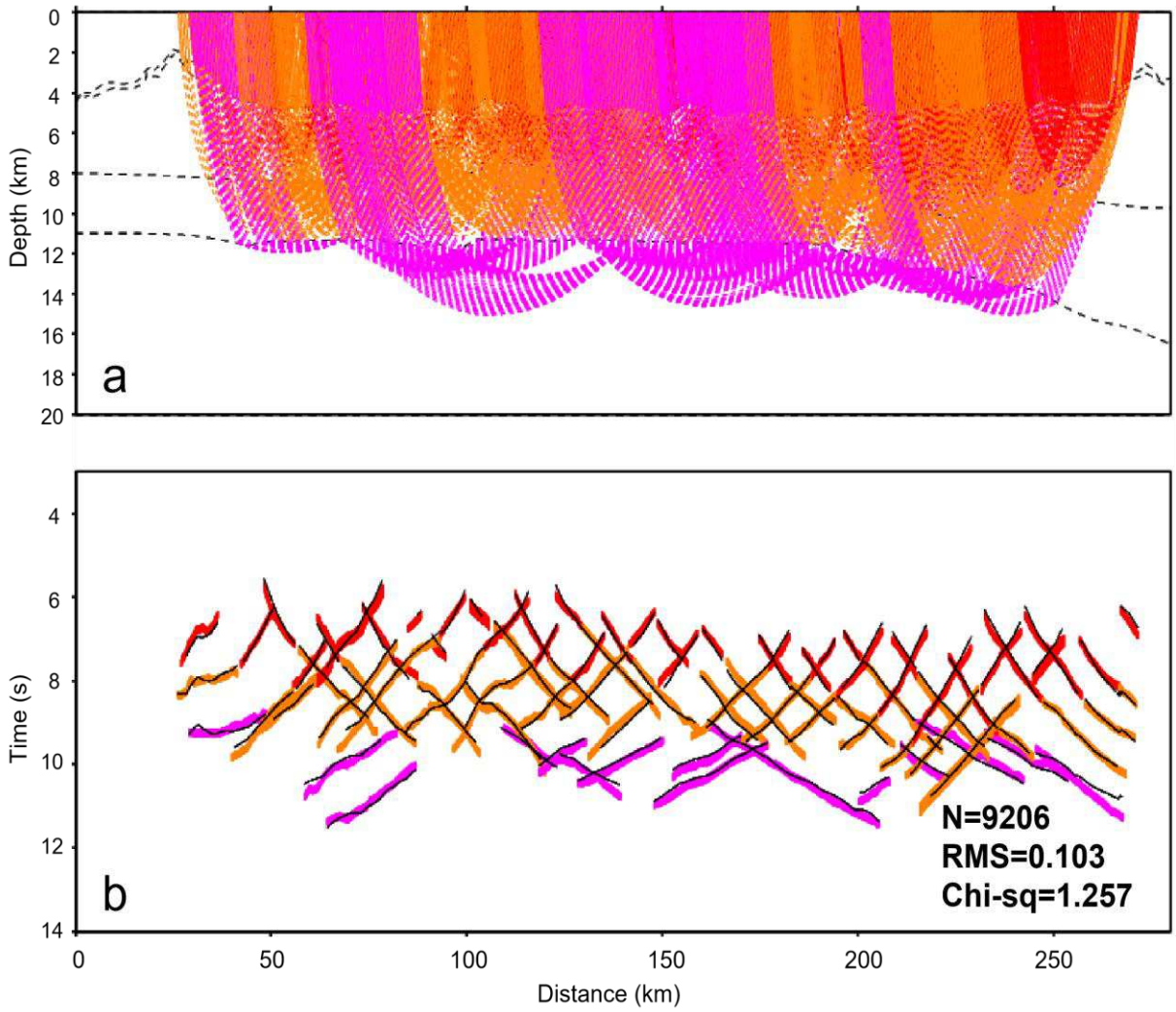

194

195 Figure 9. (a) Ray paths for all PSS converted S-wave phases. (b) Observed (colored) and calculated (black) travel-time
196 for PSS phases.

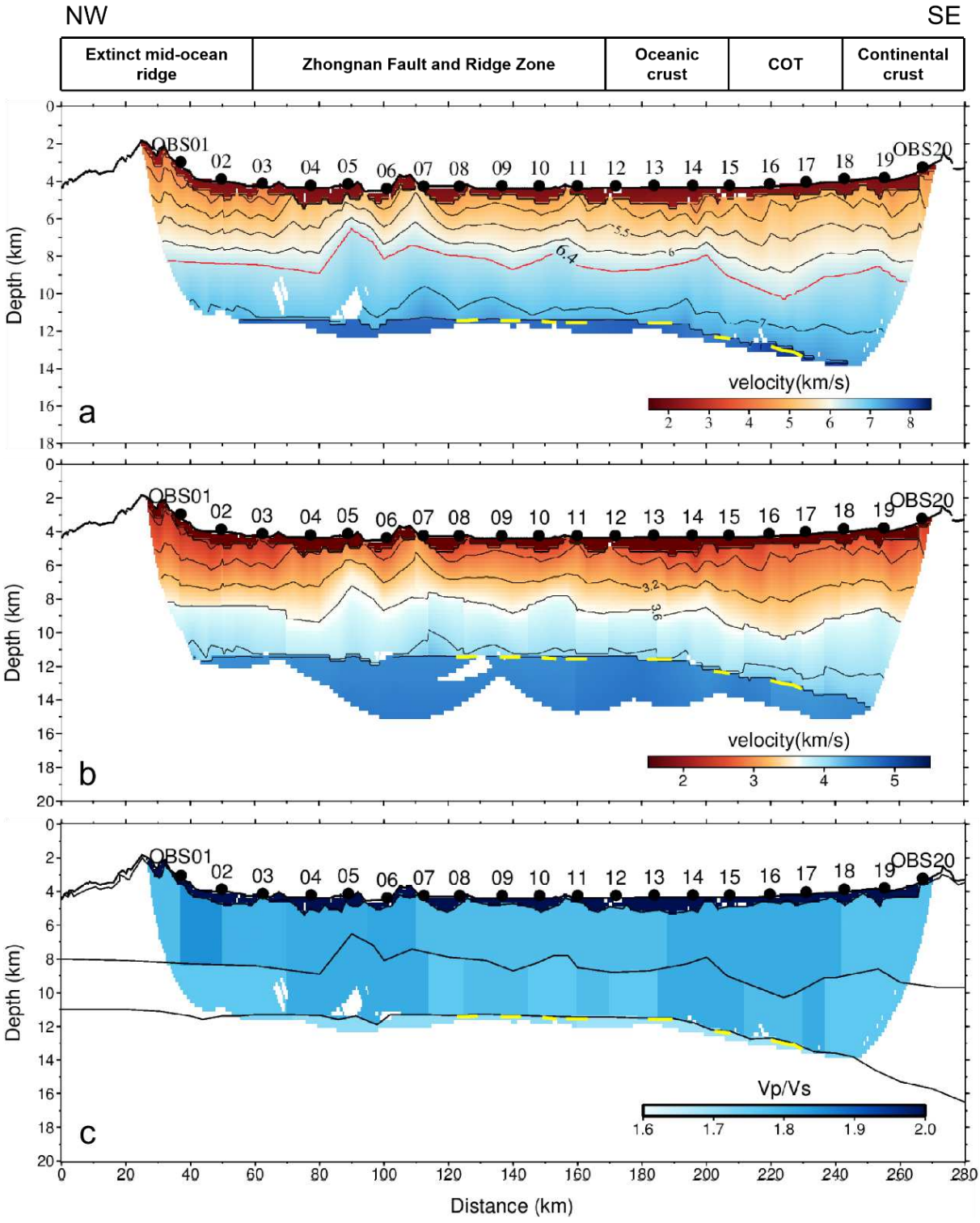

Figure 10. (a) Forward P-wave velocity model (Li et al. 2026). Numbered black dots indicate OBS locations. (b) Forward S-wave velocity model. (c) Forward Vp/Vs model. The yellow dashed line marks the Moho from Li et al. (2026).

4.3 S-wave inversion modeling

RayInvr ray-tracing forward modeling provides only approximate blockwise estimates of Vs and Vp/Vs, with low model resolution and high uncertainty. We here apply Tomo2D tomography (Korenaga et al. 2000) to better constrain the Vs velocity structure. Converted S-wave paths are asymmetric because the waves

initially propagate as P-waves and subsequently as S-waves toward the receiver. These arrivals cannot be used directly in Tomo2D and require a static travel-time correction. PPS-type waves travel as S-waves only through the sedimentary section on their upgoing paths to the receivers. Their paths nearly coincide with those of the corresponding Pg waves, but their sedimentary travel-time differ by T_d. Subtracting T_d from the travel-time of PSS waves converted at the sediment–basement interface yields equivalent PSP travel-time, for which S-wave propagation is confined to the region below basement. The correction is $T_d = T_{PPS} - T_P = T_{PSS} - T_{PSP}$. PSP paths are symmetric and can then be used in Tomo2D tomography (Li et al. 2021a, 2022; Contreras-Reyes et al. 2023; Guo et al. 2023).

Wen et al. (2024) compared two converted S-wave travel-time-correction strategies in the northeastern South China Sea: (1) subtracting the observed traveltime difference between PPSb and Pg arrivals from PSS traveltimes to obtain equivalent PSP′ arrivals, with P-wave propagation through the sediments and S-wave propagation below the sedimentary basement and, (2) using model-derived P- and S-wave traveltime differences through the sediments to obtain equivalent seafloor-converted PSS′ arrivals, with S-wave propagation through both the sediments and the crust. The resulting Vs models differ by less than 0.15 km/s, mostly between 0 and 0.1 km/s. This indicates that corrected converted-wave travel-time can support stable Vs tomography when the conversion interface and shallow velocities are adequately constrained. Wen et al. (2024) also showed that sedimentary velocities are a primary control on S-wave ray tracing. Accordingly, we use the pre-existing P-wave model to constrain sedimentary velocities and the sediment–basement interface, and correct PSS travel time using the sedimentary travel-time difference between P and PPS waves. This reduces the influence of asymmetric shallow propagation paths on the inversion for Vs below basement.

To ensure consistency in the derived Vp/Vs ratios, the S-wave inversion used the same regularization parameters as the P-wave inversion. Horizontal and vertical grid spacings are 0.5 and 0.25 km, respectively. From the top to the bottom of the model, horizontal velocity correlation lengths increase from 2 to 3 km, and vertical correlation lengths increase from 0.2 to 3 km. The Moho correlation length is 15 km. The velocity and depth smoothing weights are 120 and 5, respectively.

The geometry and velocity structure of the sedimentary layers are derived from the pre-existing P-wave model. During the inversion, strong damping is applied to the sedimentary layers to minimize the influence of shallow velocity variations on the deep crustal structure. S-wave velocities at the top and base of the crust are assigned ranges of 2.4–3.2 km/s and 3.8–4.5 km/s, respectively. A Monte Carlo approach (Korenaga et al. 2000) is used to randomly generate 100 initial velocity models, each of which is inverted using the same inversion parameters and tomographic method. The mean velocity model and the standard deviation at each model node are then calculated from the 100 resulting models. Each inversion is terminated when χ^2 fall below 2.0 or the number of iterations exceed 20. All inverted models yield root-mean-square (RMS) travel-time residuals of less than 136 ms (Fig. 11). The uncertainty in crustal Vs, quantified by the standard deviation across the model ensemble, is generally less than 0.05 km/s. Slightly higher uncertainties occur in the deeper part of the lower crust within the Zhongnan Fault Zone, possibly reflecting structural complexity and low ray density at depth, but remain below 0.1 km/s overall (Fig. 12b–c). Because all phases used in the converted S-wave inversion are refracted arrivals traveling through the crust and upper mantle, they do not provide

sufficient constraints on Moho depth. The uncertainty in Moho depth is therefore adopted from the P-wave inversion results (Li et al. 2026).

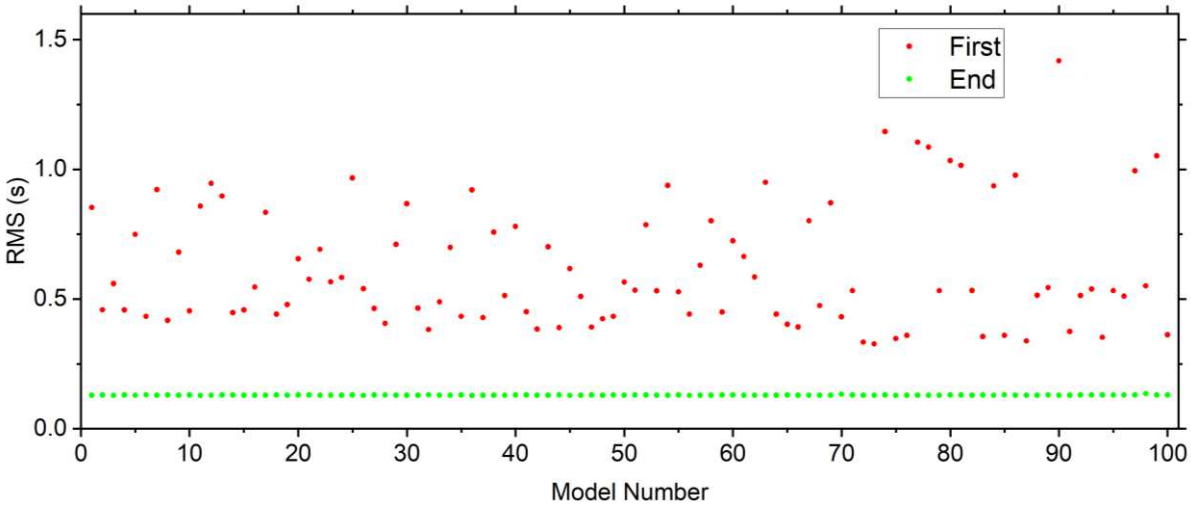

Figure 11. RMS travel-time residuals for the 100 inversion models. Red dots show residuals at the first iteration; green dots show residuals at the final iteration.

After S-wave tomography, the inverted pre-existing Vp model is divided by the mean Vs model (Fig. 12a) to obtain the Vp/Vs model (Fig. 13b). We randomly pair 100 Vs models with 100 Vp models to generate 100 Vp/Vs models and calculated the standard deviation of Vp/Vs (Fig. 13c). Uncertainty is mostly below 0.02 across of the model.

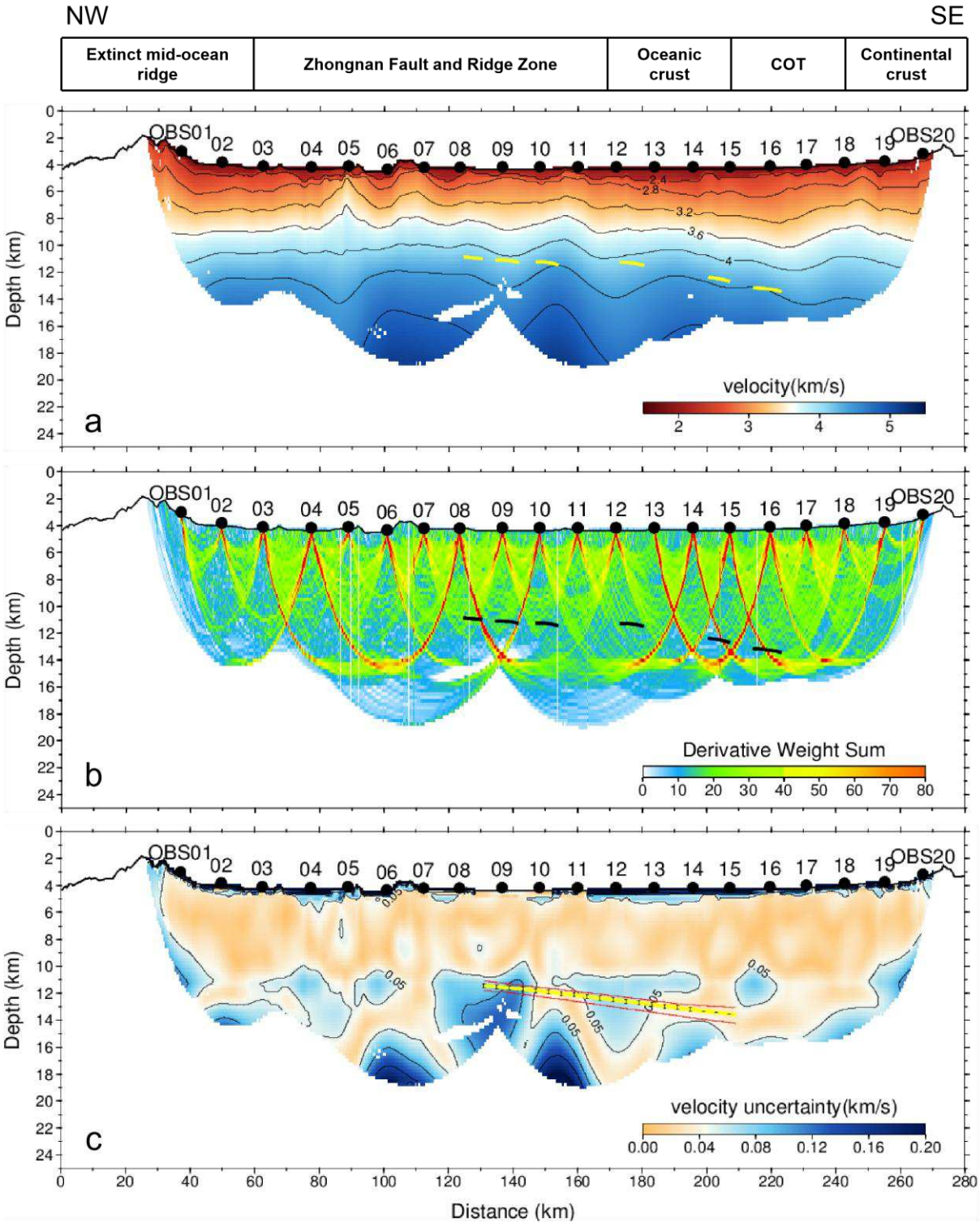

Figure 12. (a) Mean Vs model obtained using the Monte Carlo approach. The yellow dashed line marks the Moho from Li et al. (2026). (b) S-wave ray density. The black dashed line marks the interpreted Moho from Li et al. (2026). (c) Standard deviations of Vs about the mean model and of Moho depth. The yellow line represents the average Moho reflector and the black error bars represent the uncertainty of the Moho depth from Li et al. (2026).

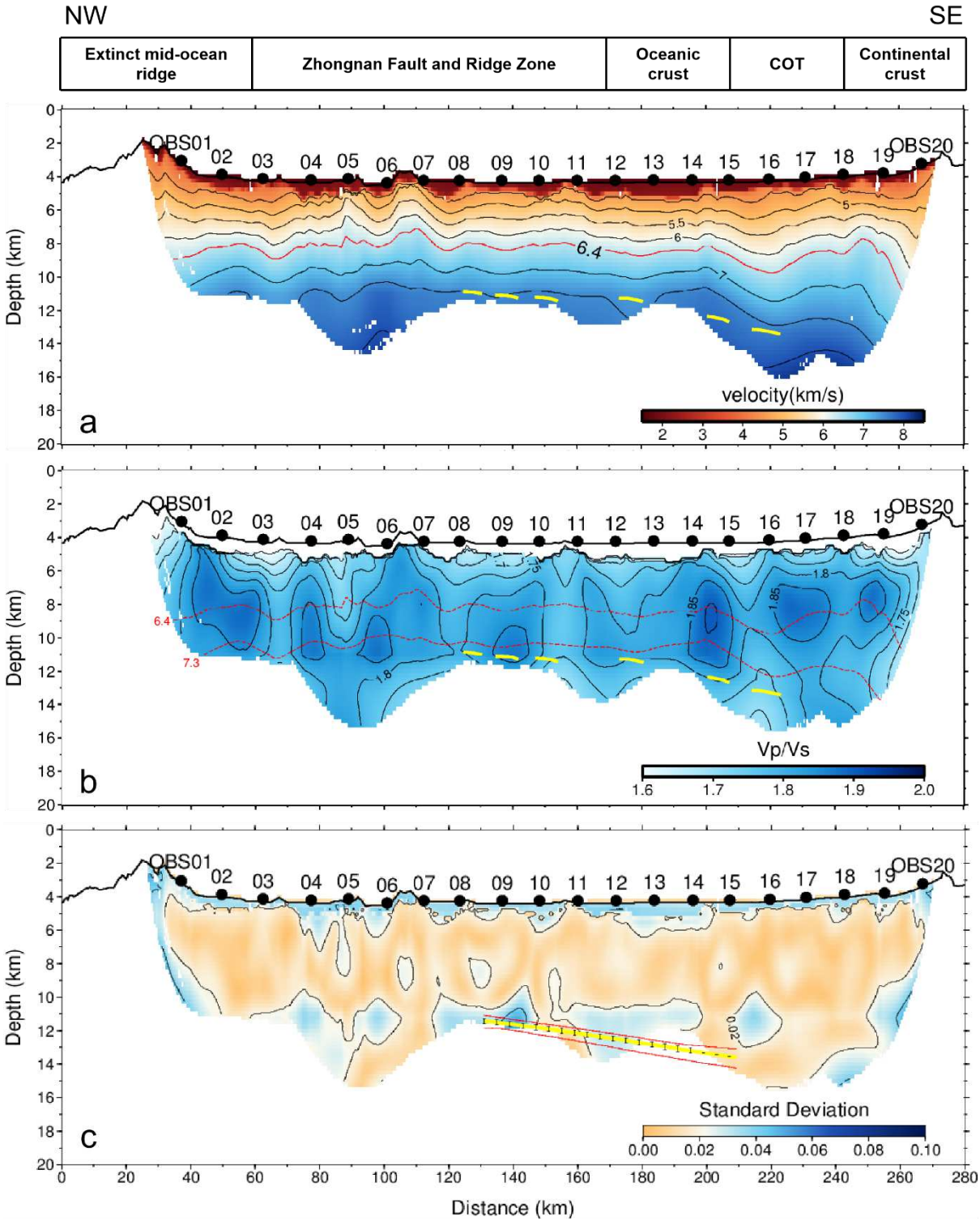

Figure 13. (a) Vp model. (b) Vp/Vs model. Red dashed lines show the positions of the 6.4 and 7.3 km/s contours in the Vp model of Li et al. (2026). The yellow dashed line marks the interpreted Moho from Li et al. (2026). (c) Standard deviations of Vp/Vs and Moho depth. The yellow line represents the average Moho reflector and the black error bars represent the uncertainty of the Moho depth from Li et al. (2026).

4.4 Resolution test

Checkerboard tests are performed to assess the spatial resolution of the inverted model. Alternating velocity perturbations of ±5% were superimposed on the average Vs model while retaining the original model node spacing. Three checkerboard patterns were constructed with individual cell sizes of 25 km × 10 km, 15 km × 8 km, and 12.5 km × 5 km (Fig. 14a–c). Synthetic travel-time were calculated by forward modeling through the perturbed models using the same source–receiver geometry as the observed data. Random noise ranging from −40 to 40 ms was added to the synthetic travel-time to simulate picking errors. The noise-contaminated synthetic travel-time were then inverted using the unperturbed average Vs model as the starting model to evaluate the recovery of the checkerboard patterns at each spatial scale. The results show that the imposed perturbations are best recovered in the crust, where ray coverage is densest, whereas 12.5 × 5 km anomalies are only partially recovered in the upper mantle and near the model boundaries owing to limited ray coverage (Fig. 14d–f).

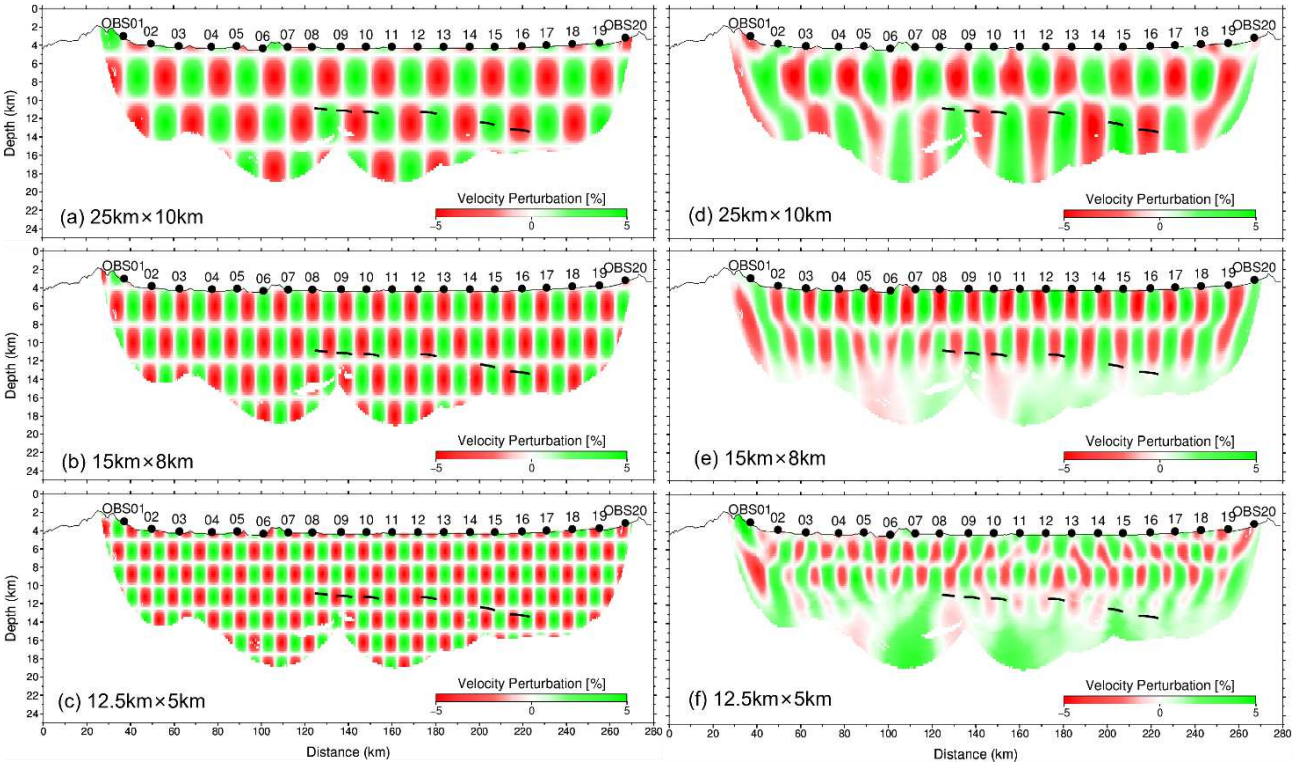

Figure 14. Checkerboard resolution tests at three spatial scales. (a), (b), and (c) present the input velocity perturbation anomaly model with patterns of 25 km × 10 km, 15 km × 8 km, 12.5 km × 5 km, respectively. Corresponding to the input model setting on the left, (d), (e), and (f) on the right show the recovered checkerboard results. Velocity perturbations of ±5% are used in all tests.

5 S-wave velocity and Vp/Vs ratio

The S-wave velocity model exhibits vertical stratification. Sedimentary Vs is approximately 0.2–0.9 km/s, whereas upper- and lower-crustal Vs ranges are 2.4–3.6 and 3.6–4.4 km/s, respectively, with local values above 4.0 km/s in the deep crust. Spatial variations in Vs correspond closely to major interfaces and anomalous Vp regions, although lateral variations are more pronounced within and around the Zhongnan Fault and Ridge Zone.

Sedimentary Vp/Vs generally exceeds 2.5, consistent with commonly reported unconsolidated marine sediments (Au and Clowes 1984; Kodaira et al. 1996; Digranes et al. 1998; Breivik et al. 2003). Crustal and upper-mantle Vp/Vs are mainly between 1.70 and 1.90. Beneath the extinct ridge, Vs ranges from 2.4 to 4.0 km/s, while Vp/Vs exhibits a block-like pattern with pronounced lateral variations and locally exceeds 1.85. In the oceanic crustal domain, Vs ranges from 2.4 to 4.3 km/s, with a high-velocity body (Vs > 4.0 km/s) near the COT. Vp/Vs is mainly 1.75–1.90 and exceeds 1.80 within the high-velocity body.

In contrast, the Zhongnan Fault and Ridge Zone is substantially more heterogeneous. Crustal Vs ranges from 2.4 to 4.4 km/s. Pronounced undulations in Vs define distinct structures, including a local upper-crustal high-velocity structure between OBS04 and OBS07. Velocity undulations become more pronounced in the deep crust near the Moho and at the top of the upper mantle, where Vs locally exceeds 4.0 km/s. Correspondingly, Vp/Vs in the crust varies strongly both laterally and vertically. Crustal ratios are mainly 1.70–1.90, with local high-Vp/Vs zones (>1.80) extending upward from depth, in places reaching the sediment–basement interface. Another high Vp/Vs region occurs chiefly in the lower crust, with local values above 1.85. The Zhongnan Fault and Ridge Zone is thus one of the most structurally heterogenous parts on the profile.

The COT adjacent to the continental Reed Bank differs from the Zhongnan Fault and Ridge Zone in its velocity structure. Crustal Vs ranges from 2.4 to 4.3 km/s and Vp/Vs from 1.70 to 1.90. From the oceanic toward the continental domain, Vs generally decreases, whereas Vp/Vs follows a distinct high–low–high lateral pattern. Vp/Vs ratios are relatively high on the oceanic side, decrease in the central COT, and rise again toward the Reed Bank, where the high ratios are concentrated mainly in the upper crust. Beneath the Reed Bank, both Vs and Vp/Vs are generally lower than in the adjacent oceanic crust, and velocity stratification between the upper and lower crust is well defined. The lateral changes in Vs and Vp/Vs from the oceanic crust through the COT to Reed Bank show substantial lateral heterogeneity within the COT. Overall, both Vp and Vs models resolve pronounced structural variations within both the Zhongnan Fault and Ridge Zone and COT, whereas the normal oceanic crust exhibit more continuous velocity structures.

6 Discussion

6.1 Lithological implications

In the extinct spreading ridge, the Zhongnan Fault and Ridge Zone, and normal oceanic crust, upper crustal Vp versus Vs plot mainly within the velocity range of basalt (Fig. 15a), whereas lower crustal Vp versus Vs fall predominantly within the ranges of diabase and gabbro, consistent with the typical vertical lithological stratification of oceanic crust. Upper oceanic crust has typical velocities of Vp = 4.0–6.5 km/s and Vs = 2.0–3.5 km/s, and Vp/Vs ratios generally between 1.70 and 2.10 (Bullock and Minshull 2005). Lower oceanic crust has higher velocities of Vp > 6.5 km/s and Vs > 3.5 km/s and Vp/Vs ratios mainly between 1.70 and 1.90 (Carlson and Miller 1997; Carlson and Jay Miller 2004; Grevemeyer et al. 2018b). The Vs and Vp/Vs obtained in this study agree closely with these representative rock properties; from the top to the base of the oceanic crust, Vp/Vs and the associated velocity combinations indicate a progressive lithological transition

from basalt to diabase and gabbro, consistent with the composition represented in classical oceanic crustal models (White et al. 1992; Grevemeyer et al. 2018b).

The Vp–Vs relationships within the COT adjacent to the Reed Bank indicate lithological characteristics distinct from those of typical oceanic or continental crust (Fig. 15b). The upper crust is mainly consistent with andesite of continental affinity and oceanic basalt, whereas the lower crust is primarily consistent with diabase, gabbro, amphibolite, and mafic granulite, with some samples approaching the velocity range of metapelite. This complex distribution indicates a mixed lithological assemblage and a crustal structure shaped by continental breakup, oceanic crustal accretion, and subsequent magmatism. The coexistence of continental andesitic and oceanic basaltic affinities in the upper crust of the COT suggests that the shallow crust retains remnant continental or continental-margin volcanic rocks, as well as basaltic eruptions during seafloor spreading, reflecting the progressive transition from continental to oceanic crust. The lower crustal lithologies suggest substantial modification by metamorphism and mafic underplating during the late stages of breakup. The few samples close to the metapelite velocity range may indicate that remnants of continental material in the deep COT. Overall, the COT adjacent to the Reed Bank is neither magma-poor nor volcanic. This interpretation is broadly consistent with previous evidence for localized magmatic underplating and complex continent–ocean transitional structure near the Reed Bank (Franke 2013; Peng et al. 2020; Guo et al. 2023; Li et al. 2026).

In the continental domain, samples from the uppermost crust plot mainly within the velocity field of andesite, whereas those from the lower part of the upper crust correspond predominantly to felsic rocks such as granodiorite and granite. The lower crust is mainly consistent with greenschist- and amphibolite-related lithologies, defining an overall lithological transition from shallow intermediate–felsic rocks to mafic metamorphic rocks at depth (Fig. 15c). These inferred lithologies are consistent with those identified along nearby profiles in the study area and within the Zhongsha Block (Wei et al. 2015, 2017; Li et al. 2021a, 2022; Guo et al. 2023), supporting a relatively well-preserved continental domain in the study area.

The predominance of andesite-like velocity characteristics in the uppermost crust suggests the possible presence of margin-related intermediate volcanic rocks, whose formation may have been closely associated with prolonged Mesozoic subduction and late-stage extension. Felsic intrusive rocks such as granodiorite and granite in the lower part of the upper crust are important constituents of continental crust and are indicative of a granitic basement, suggesting that relatively mature continental crust had developed prior to breakup and that substantial felsic crustal components were preserved during subsequent extensional thinning. Localized structures with $Vp/Vs > 1.80$ are also present within the middle to upper crust. Considering their Vp and Vs characteristics, together with their spatial association with the adjacent COT and structurally weak zones, these high Vp/Vs anomalies may reflect variable degrees of mafic magmatic modification of the pre-existing intermediate–felsic continental crust. During continental breakup and subsequent extension, mafic magma may have migrated upward along margin faults or structurally weak zones within the COT and intruded into the middle to upper crust, locally increasing the mafic component of the crust and elevating Vp/Vs. Less modified domains may have retained part of their original felsic continental crustal character. The continental

crust in this region therefore more likely represents a heterogeneous assemblage produced by the interaction between pre-existing felsic continental crust and later mafic magmatic intrusion, rather than a uniform domain.

Frost and Frost. (2013) emphasized that metamorphic mineral assemblages should be interpreted in the context of protolith composition together with pressure–temperature–fluid (P–T–fluid) conditions. The greenschist- and amphibolite-like velocity characteristics identified in this study are reasonably interpreted as the products of mafic igneous protoliths that underwent variable degrees of metamorphism in response to magmatic heating and fluid activity. The inferred lithologies in this study closely resemble those identified in the middle and lower crust beneath the Zhongsha Block on the conjugate margin (Li et al. 2022) and are also broadly consistent with the magmatic modification inferred by the Vp/Vs model in this study.

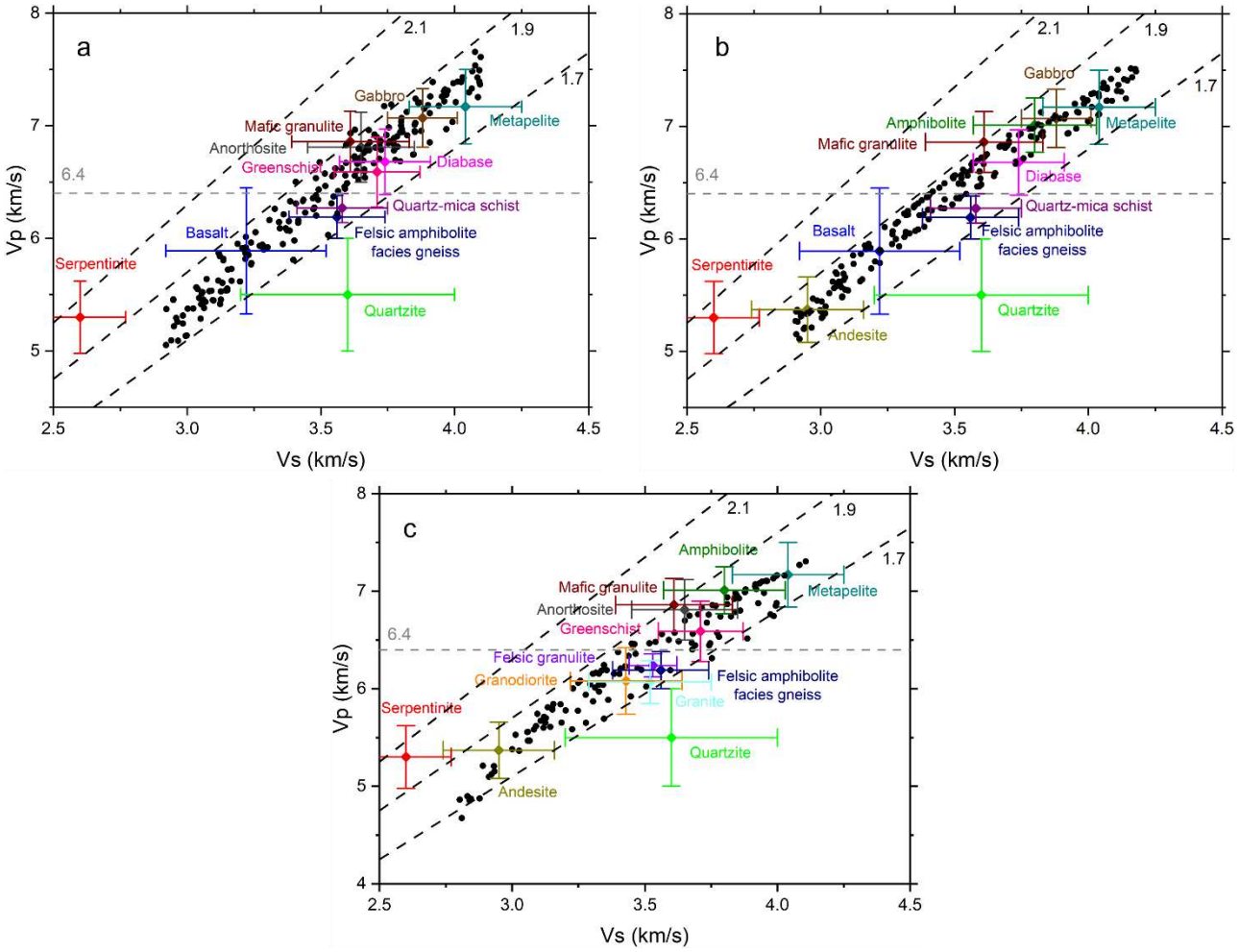

Figure 15. Comparison of modeled Vp–Vs relationships with reference lithologies for (a) oceanic crust, (b) the COT, and (c) continental crust. Rock-property data are from Christensen and Mooney (1995) and Christensen (1996), corrected by Li et al. (2022) to pressures of 200–600 MPa according to their inferred depths, shown by different colored circles. The black dots represent the sampling points in our model.

6.2 Nature of the anomalous velocity structures

Several high-velocity bodies occur in the lower crust and near the Moho, their joint Vp, Vs, and Vp/Vs characteristics are similar, suggesting that they may originate from the same source. Most have high Vp (>7.3 km/s) and Vs (>4.0 km/s), with Vp/Vs mainly between 1.80 and 1.90, resembling those of mafic rocks such

as gabbro and diabase (Fig. 16) (Carlson and Miller 1997; Carlson and Jay Miller 2004; Grevemeyer et al. 2018b). We therefore favor interpreting most of these bodies as products of mafic magmatic underplating, potentially forming a predominantly gabbroic lower crust. This interpretation is consistent with the pronounced tectonic and magmatic activity near the Zhongnan Fault and Ridge Zone and suggests that deep faults facilitated the migration and accumulation of mafic magma within the crust.

A high-Vp/Vs zone beneath OBS06 and OBS07 extends upward from the deep crust and connects with a shallow volcanic structure. This feature may indicate the extent of magma migration. Faults may be abundant in this region owing to the combined effects of tectonic and magmatic activity. Associated deep faults could also have provided pathways for downward seawater infiltration. We randomly picked velocities from the high-velocity bodies in the bottom of this zone and found most of them fell within the velocity ranges corresponding to serpentinite and gabbro/diabase (Fig. 16). Evident Moho reflection also lacks in this region. These evidences argue for the presence of serpentinized mantle peridotite. Jiang et al. (2025) identified ~ 3.3–4.3 km thick of oceanic crust and Vp/Vs > 1.90 beneath the extinct spreading ridge in the East Sub-basin, and linked these features to declining magma supply and increasing mantle hydration during terminal spreading. Fault-controlled seawater infiltration may also have occurred within the Zhongnan Fault and Ridge Zone. However, the overlapping seismic properties of gabbro and serpentinite prevent a unique lithological interpretation. Localized mantle hydration is therefore considered as a possible process accompanying fault-controlled magmatic modification within the Zhongnan Fault and Ridge Zone.

The high-velocity anomalies in the study area may therefore have spatially variable origins. Fault-controlled magma migration and seawater infiltration may have been locally coupled, jointly modifying the composition and seismic properties of the deep crust and upper mantle.

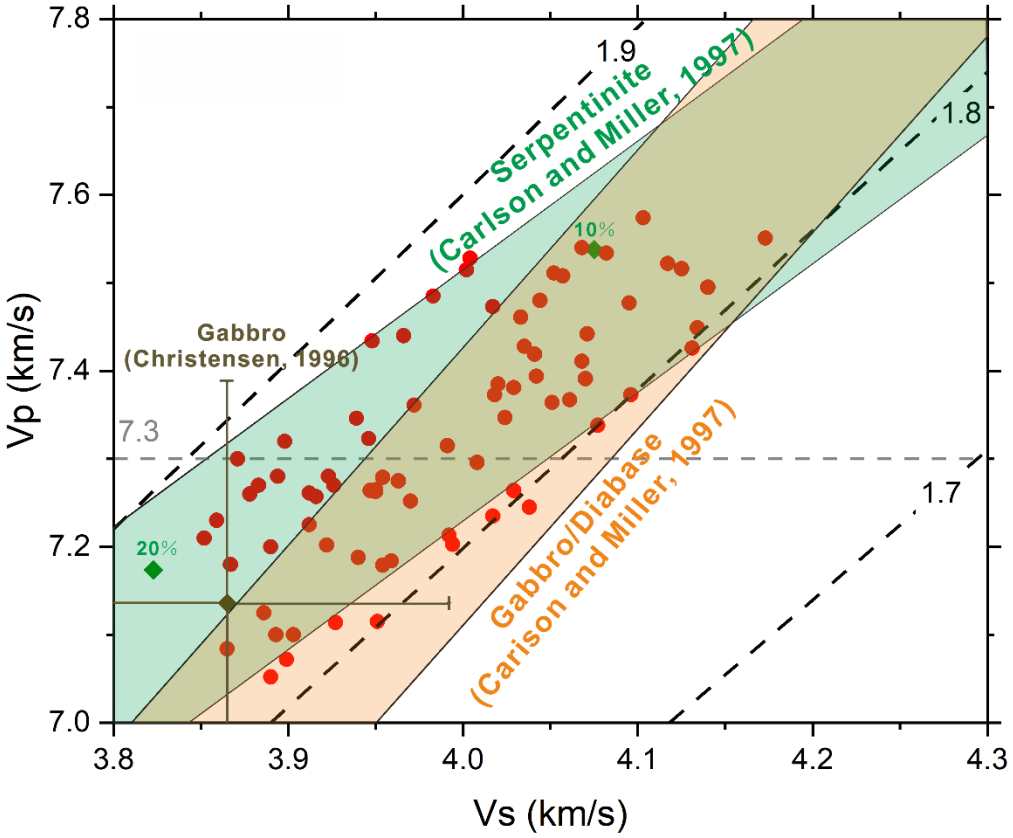

Figure 16. Vp/Vs ratio in the high-velocity bodies. The numbers on the black dotted line represent the Vp/Vs ratio. The transparent green and orange regions represent the laboratory velocity ranges for serpentinite and gabbro/diabase (Carlson and Miller 1997), respectively. The green diamonds mark the serpentinization degrees (Carlson 2001). The brown diamond with the error bar marks the velocity range of gabbro (Christensen 1996). The red dots represent the sampling points within the high-velocity bodies. All the laboratory data were measured under a confining pressure of 200 MPa (Li et al. 2021a).

6.3 Implications for Tectono-Magmatic Evolution

Interactions among tectonic deformation, magma supply, and crustal mechanical properties jointly controlled crustal evolution from margin extension through the continent–ocean transition to seafloor spreading. The combined Vp, Vs, and Vp/Vs models reveal pronounced lateral heterogeneity in crustal structure, most notably within the Zhongnan Fault and Ridge Zone and the Reed Bank COT. Strongly undulating Vp and Vs and multiple high-Vp/Vs structures within the Zhongnan Fault and Ridge Zone indicate substantial tectonic modification and magmatic activity. Together with the lower-crustal high-velocity bodies and localized crustal thickening in P-wave studies, these velocity anomalies may record mafic intrusion and lower-crustal modification controlled by transform structures. Faults and associated zones of weakness have accommodated relative motion between spreading segments and provided pathways for magma migration upward. The Zhongnan Fault and Ridge Zone may thus have been an important locus of coupled tectonic deformation and magmatic accretion during the formation of the Southwest Sub-basin (Fig. 17).

The COT exhibits a spatially heterogeneous magmatic imprint. Relatively large high-Vp/Vs structures (>1.85) occur on its oceanic side, but become smaller and are concentrated mainly in the upper crust toward the continental crust of the Reed Bank. This seaward–landward asymmetry reflect mechanical controls on magma supply and intrusion: magma preferentially accumulated and intruded in the weaker seaward domain, whereas stronger landward basement limited its lateral distribution. Previously identified lower-crustal high-velocity bodies and localized underplating near the Reed Bank COT support this interpretation (Peng et al. 2020; Guo et al. 2023). Vertical Vp/Vs bands exceeding 1.80 also link the upper mantle to the shallow crust within the COT, indicating upward magma migration along structural weaknesses and localized modification of the upper crust (Fig. 17).

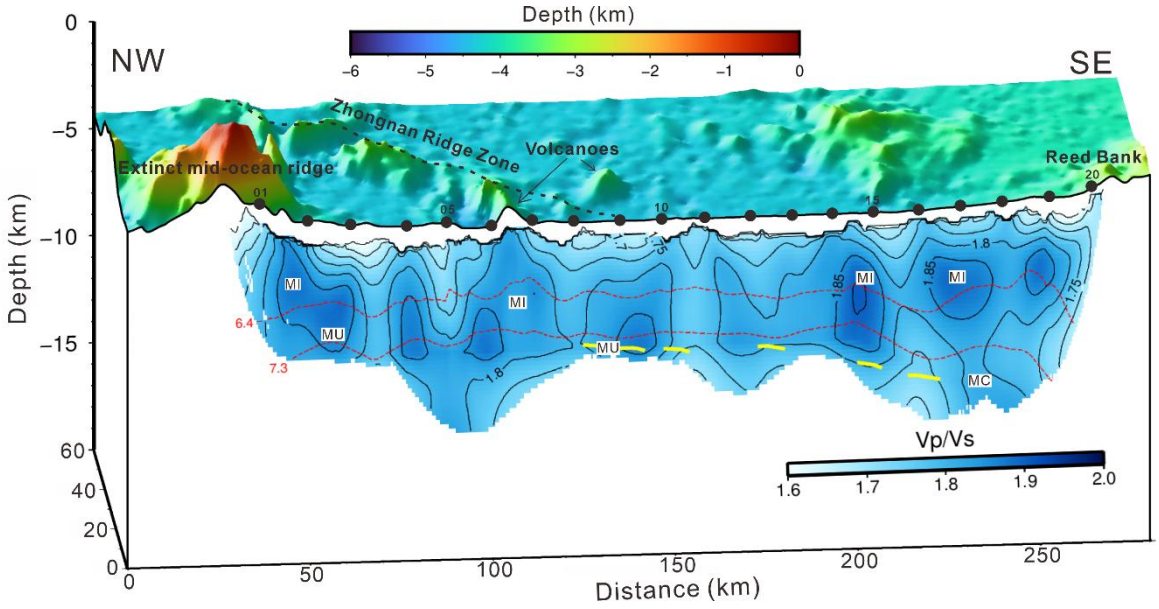

Figure 17. Three-dimensional bathymetry near the seismic profile OBS2023-1 and the Vp/Vs structure. Red dashed lines show the positions of the 6.4 and 7.3 km/s contours in the Vp model of Li et al. (2026). The yellow dashed line marks the Moho from Li et al. (2026). MU, magmatic underplating; MI, magmatic intrusions; MC, magmatic conduits.

7 Conclusions

Crossing the Zhongnan Fault and Ridge Zone from the relict mid-ocean ridge southwards to the southern continental margin of the South China Sea, we derived an S-wave velocity structure along the ocean bottom seismic profile OBS2023-1 from converted S-waves, and combined it with the pre-existing P-wave velocity structure (Li et al. 2026) to construct a Vp/Vs section. The integrated analysis yields the following conclusions:

1. Sedimentary Vs is approximately 0.2–0.9 km/s, and upper and lower crustal Vs values are mainly 2.4–3.6 and 3.6–4.4 km/s, respectively. Vp/Vs is mainly between 1.70 and 1.90. The Vs model corresponds well with the recently obtained Vp model of the same profile in major structural interfaces and velocity anomalies. The Zhongnan Fault and Ridge Zone and COT exhibit stronger lateral heterogeneity than the typical oceanic basin of the South China Sea.

2. Vp–Vs relationships conform with typical basalt–diabase–gabbro stratification in the oceanic crust; in the study area, the continental crust is composed of felsic rocks such as andesite and granite at shallow depths and mafic rocks such as greenschist or amphibolite at greater depths. The COT adjacent to the Reed Bank exhibits a composite lithology with coexisting continental and oceanic components; its lower crust is mainly consistent with mafic lithologies including diabase, gabbro, amphibolite, and mafic granulite. This assemblage reflects the combined effects of continental breakup and magmatic modification on the original continental-margin crust.

3. Most high-velocity anomalies in the lower crust and near the Moho combine high Vp and Vs with Vp/Vs of 1.80–1.90, resembling those of mafic rocks such as gabbro and diabase. They are most consistent with mafic lower crustal intrusion and, locally, magmatic underplating. The high-Vp/Vs zone beneath OBS06 and OBS07 connects with a shallow volcanic structure and may indicate the extent of magma migration. Associated deep faults may also have facilitated seawater infiltration and localized mantle hydration near the lower end of this band. However, the overlapping seismic properties of gabbro and partially serpentinized peridotite prevent a unique lithological interpretation

4. Vp, Vs, and Vp/Vs together identify the Zhongnan Fault and Ridge Zone as an important locus of coupled tectonic deformation and magmatic modification, where transform faulting along the zone may have controlled deep magma/fluid migration and crustal modification. The Reed Bank COT records marked seaward–landward asymmetry in magmatism: larger high Vp/Vs structures and vertically connected Vp/Vs zones on the seaward side indicate stronger magmatic modification, whereas modification on the landward side was more limited. In contrast to previous studies focused on hydration at individual extinct spreading ridges or local COT structure, this study compares Vs and Vp/Vs across an extinct spreading center, transform structures, normal oceanic crust, and the COT along one continuous profile.

Acknowledgments Seismic data were collected during the open research voyage NORC2023-08. We sincerely thank Captain, the crew, and the scientific team aboard the R/V “Experiment 6” for their invaluable efforts during the expedition.

Author contributions W.S.: Writing – original draft, Software, Methodology, Investigation, Data curation. C.L.: Writing – review & editing, Supervision, Investigation, Funding acquisition, Conceptualization. W.L.: Resources, Investigation. Y.Y.: Resources, Investigation. M.X.: Investigation. C.Y.: Investigation. Y.D.: Software. M.Y.: Resources. J.G.: Investigation.

Funding This work was supported by the National Natural Science Foundation of China under contracts No. 42576050 and 42276066, and by the National Key Research and Development Program of China under contract No. 2023YFF0803404.

Data availability Data will be made available on request.

Declarations

Competing interest The authors declare that they have no known competing financial interests or personal relationships that could have appeared to influence the work reported in this paper.

References

Au D, Clowes RM (1984) Shear-wave velocity structure of the oceanic lithosphere from ocean bottom seismometer studies. Geophys J Int 77:105–123. https://doi.org/10.1111/j.1365-246X.1984.tb01927.x

Barckhausen U, Engels M, Franke D, et al (2014) Evolution of the South China Sea: Revised ages for breakup and seafloor spreading. Mar Pet Geol 58:599–611. https://doi.org/10.1016/j.marpetgeo.2014.02.022

Breivik AJ, Mjelde R, Grogan P, et al (2003) Crustal structure and transform margin development south of Svalbard based on ocean bottom seismometer data. Tectonophysics 369:37–70. https://doi.org/10.1016/S0040-1951(03)00131-8

Briais A, Patriat P, Tapponnier P (1993) Updated interpretation of magnetic anomalies and seafloor spreading stages in the south China Sea: Implications for the Tertiary tectonics of Southeast Asia. J Geophys Res Solid Earth 98:6299–6328. https://doi.org/10.1029/92JB02280

Bullock AD, Minshull TA (2005) From continental extension to seafloor spreading: crustal structure of the Goban Spur rifted margin, southwest of the UK. Geophys J Int 163:527–546. https://doi.org/10.1111/j.1365-246X.2005.02726.x

Carlson RL (2001) The abundance of ultramaÆc rocks in Atlantic Ocean crust

Carlson RL, Jay Miller D (2004) Influence of pressure and mineralogy on seismic velocities in oceanic gabbros: Implications for the composition and state of the lower oceanic crust. J Geophys Res Solid Earth 109:2003JB002699. https://doi.org/10.1029/2003JB002699

Carlson RL, Miller DJ (1997) A new assessment of the abundance of serpentinite in the oceanic crust. Geophys Res Lett 24:457–460. https://doi.org/10.1029/97GL00144

Chang J-H, Hsieh H-H, Mirza A, et al (2017) Crustal structure north of the Taiping Island (Itu Aba Island), southern margin of the South China Sea. J Asian Earth Sci 142:119–133. https://doi.org/10.1016/j.jseaes.2016.08.005

Christensen NI (2004) Serpentinites, Peridotites, and Seismology. Int Geol Rev 46:795–816. https://doi.org/10.2747/0020-6814.46.9.795

Christensen NI (1996) Poisson's ratio and crustal seismology. J Geophys Res Solid Earth 101:3139–3156. https://doi.org/10.1029/95JB03446

Christensen NI, Mooney WD (1995) Seismic velocity structure and composition of the continental crust: A global view. J Geophys Res Solid Earth 100:9761–9788. https://doi.org/10.1029/95JB00259

Contreras-Reyes E, Obando-Orrego S, Grevemeyer I (2023) 2-D V p and V s Models of the Indian Oceanic Crust Adjacent to the NinetyEast Ridge. J Geophys Res Solid Earth 128:e2022JB025701. https://doi.org/10.1029/2022JB025701

Digranes P, Mjelde R, Kodaira S, et al (1998) A regional shear-wave velocity model in the central Vøring Basin, N. Norway, using three-component Ocean Bottom Seismographs. Tectonophysics 293:157–174. https://doi.org/10.1016/S0040-1951(98)00093-6

Franke D (2013) Rifting, lithosphere breakup and volcanism: Comparison of magma-poor and volcanic rifted margins. Mar Pet Geol 43:63–87. https://doi.org/10.1016/j.marpetgeo.2012.11.003

Frost BR, Frost CD Essentials of Igneous and Metamorphic Petrology

Grevemeyer I, Hayman NW, Peirce C, et al (2018a) Episodic magmatism and serpentinized mantle exhumation at an ultraslow-spreading centre. Nat Geosci 11:444–448. https://doi.org/10.1038/s41561-018-0124-6

Grevemeyer I, Ranero CR, Ivandic M (2018b) Structure of oceanic crust and serpentinization at subduction trenches. Geosphere 14:395–418. https://doi.org/10.1130/GES01537.1

Guo J, Qiu X, Huang H, et al (2023) S-wave velocity structure and Vp/Vs ratios beneath Liyuexi Trough, Nansha Block, the South China Sea: Implications for crustal lithology and tectonic nature of the southern continental margin. Tectonophysics 869:230103. https://doi.org/10.1016/j.tecto.2023.230103

Jiang H, Huang H, He E, et al (2025) Hydration in the Crust and Upper Mantle Near the Extinct Spreading Ridge in the Eastern Sub-Basin, South China Sea. Geophys Res Lett 52:e2025GL115670. https://doi.org/10.1029/2025GL115670

Kodaira S, Bellenberg M, Iwasaki T, et al (1996) Vp IVs ratio structure of the Lofoten continental margin, northern Norway, and its geological implications. Geophys J Int 124:724–740. https://doi.org/10.1111/j.1365-246X.1996.tb05634.x

Korenaga J, Holbrook WS, Kent GM, et al (2000) Crustal structure of the southeast Greenland margin from joint refraction and reflection seismic tomography. J Geophys Res Solid Earth 105:21591–21614. https://doi.org/10.1029/2000JB900188

Li C, Song T (2012) Magnetic recording of the Cenozoic oceanic crustal accretion and evolution of the South China Sea basin. Chin Sci Bull 57:3165–3181. https://doi.org/10.1007/s11434-012-5063-9

Li C, Xu X, Lin J, et al (2014) Ages and magnetic structures of the South China Sea constrained by deep tow magnetic surveys and IODP Expedition 349. Geochem Geophys Geosystems 15:4958–4983. https://doi.org/10.1002/2014GC005567

Li J (1997) The Rifting and Collison of The South China Sea Terrain System. In: Marine Geology and Palaeoceanography. CRC Press

Li W, Li C-F, Yao Y, et al (2026) P-wave velocity structure of the Zhongnan Fault and Ridge Zone between two sub-basins of the South China Sea. Tectonophysics 937:231369. https://doi.org/10.1016/j.tecto.2026.231369

Li Y, Grevemeyer I, Huang H, et al (2021a) Seismic Constraint From Vp / Vs Ratios on the Structure and Composition Across the Continent-Ocean Transition Zone, South China Sea. Geophys Res Lett 48:e2021GL094656. https://doi.org/10.1029/2021GL094656

Li Y, Grevemeyer I, Huang H, et al (2022) Crustal Compositional Variations From Continental to Oceanic Domain: A V P / V S Ratio Study Across the Zhongsha Block, South China Sea. J Geophys Res Solid Earth 127:e2021JB023470. https://doi.org/10.1029/2021JB023470

Li Y, Huang H, Grevemeyer I, et al (2021b) Crustal structure beneath the Zhongsha Block and the adjacent abyssal basins, South China Sea: New insights into rifting and initiation of seafloor spreading. Gondwana Res 99:53–76. https://doi.org/10.1016/j.gr.2021.06.015

Mjelde R, Raum T, Digranes P, et al (2003) Vp/Vs ratio along the Vøring Margin, NE Atlantic, derived from OBS data: implications on lithology and stress field. Tectonophysics 369:175–197. https://doi.org/10.1016/S0040-1951(03)00198-7

Peng X, Li C-F, Shen C, et al (2020) Anomalous lower crustal structure and origin of magmatism in the southeastern margin of the South China Sea. Mar Pet Geol 122:104711. https://doi.org/10.1016/j.marpetgeo.2020.104711

Pichot T, Delescluse M, Chamot-Rooke N, et al (2014) Deep crustal structure of the conjugate margins of the SW South China Sea from wide-angle refraction seismic data. Mar Pet Geol 58:627–643. https://doi.org/10.1016/j.marpetgeo.2013.10.008

Qiu X, Zhao M, Ao W, et al (2011) OBS survey and crustal structure of the Southwest Sub-basin and Nansha Block, South China Sea. Chin. J. Geophys. 54 (12), 3117-3128. https://doi.org/10.1002/cjg2.1680.

Sibuet J-C, Yeh Y-C, Lee C-S (2016) Geodynamics of the South China Sea. Tectonophysics 692:98–119. https://doi.org/10.1016/j.tecto.2016.02.022

Song T, Li C-F, Wu S, et al (2019) Extensional styles of the conjugate rifted margins of the South China Sea. J Asian Earth Sci 177:117–128. https://doi.org/10.1016/j.jseaes.2019.03.008

Wei X, Ruan A, Li J, et al (2017) S-wave velocity structure and tectonic implications of the northwestern sub-basin and Macclesfield of the South China Sea. Mar Geophys Res 38:125–136. https://doi.org/10.1007/s11001-016-9288-x

Wei X, Ruan A, Zhao M, et al (2015) Shear wave velocity structure of Reed Bank, southern continental margin of the South China Sea. Tectonophysics 644–645:151–160. https://doi.org/10.1016/j.tecto.2015.01.006

Wen G, Wan K, Xia S, et al (2024) Tomographic inversion of OBS converted shear waves: case study of profile EW6 in the Dongsha area. Acta Oceanol Sin 43:13–25. https://doi.org/10.1007/s13131-023-2274-7

White RS, McKenzie D, O'Nions RK (1992) Oceanic crustal thickness from seismic measurements and rare earth element inversions. J Geophys Res Solid Earth 97:19683–19715. https://doi.org/10.1029/92JB01749

Yu Z, Li J, Ding W, et al (2017) Crustal structure of the Southwest Subbasin, South China Sea, from wide-angle seismic tomography and seismic reflection imaging. Mar Geophys Res 38:85–104. https://doi.org/10.1007/s11001-016-9284-1

Zelt CA, Smith RB (1992) Seismic traveltime inversion for 2-D crustal velocity structure. Geophys J Int 108:16–34. https://doi.org/10.1111/j.1365-246X.1992.tb00836.x

Zhang J, Li J, Ruan A, et al (2020) Seismic Structure of a Postspreading Seamount Emplaced on the Fossil Spreading Center in the Southwest Subbasin of the South China Sea. J Geophys Res Solid Earth 125:e2020JB019827. https://doi.org/10.1029/2020JB019827

Zhang J, Li J, Ruan A, et al (2016) The velocity structure of a fossil spreading centre in the Southwest Sub-basin, South China Sea. Geol J 51:548–561. https://doi.org/10.1002/gj.2778

Zhang J, Li Y, Yao Y, et al (2025) Seismic Structure and the Variation of Magmatic Budget in the Southwest Sub-Basin of the South China Sea. J Geophys Res Solid Earth 130:e2025JB031304. https://doi.org/10.1029/2025JB031304

Zhao M, Qiu X, Xia S, et al (2010) Seismic structure in the northeastern South China Sea: S-wave velocity and Vp/Vs ratios derived from three-component OBS data. Tectonophysics 480:183–197. https://doi.org/10.1016/j.tecto.2009.10.004

Zhao M, Qiu X, Xia S, et al (2008) Identification and analysis of shear waves recorded by three-component OBSs in northeastern South China Sea. Prog Nat Sci 18:181–188. https://doi.org/10.1016/j.pnsc.2007.06.005